

*Digital Comprehensive Summaries of Uppsala Dissertations
from the Faculty of Science and Technology 2268*

High Bandgap FAPbBr_3 Perovskite Solar Cells

Preparation, Characterization, and Application

YAWEN LIU



ACTA UNIVERSITATIS
UPSALIENSIS
2023

ISSN 1651-6214
ISBN 978-91-513-1810-3
urn:nbn:se:uu:diva-500172



UPPSALA
UNIVERSITET

Dissertation presented at Uppsala University to be publicly examined in Högssalen, Ångströmlaboratoriet, Lägerhyddsvägen 1, Uppsala, Thursday, 8 June 2023 at 13:15 for the degree of Doctor of Philosophy. The examination will be conducted in English. Faculty examiner: Professor Tönu Pullerits (Lund University, Chemical Physics).

Abstract

Liu, Y. 2023. High Bandgap FAPbBr₃ Perovskite Solar Cells. Preparation, Characterization, and Application. *Digital Comprehensive Summaries of Uppsala Dissertations from the Faculty of Science and Technology* 2268. 87 pp. Uppsala: Acta Universitatis Upsaliensis. ISBN 978-91-513-1810-3.

High bandgap lead-halide perovskite solar cells (PSCs) have gained interest as top cells for tandem solar cells and photoelectrochemical applications due to their suitable energy bands. However, the PSCs have limited stability and performance, and their fabrication in a glovebox and utilization of expensive metal contacts increase the cost and limit their application. Therefore, this thesis aims to enhance the efficiency and stability of high bandgap formamidinium lead tri-bromide PSCs (FAPbBr₃-PSCs), simplify the preparation process, reduce their cost, and explore their application in energy conversion by optimization operation processes in an ambient environment. To achieve perovskite films of superior quality featuring large crystal sizes and high solar-to-electricity power conversion efficiency (PCE), we investigated various techniques, including adding additives and solvent engineering, in preparation of the perovskite. We also built a 2D/3D perovskite interface to passivate the interfacial defects and increase the PCE and stability of the PSCs. In addition, we compared the performance of different dopant-free hole transport materials (HTMs). We found that the polymer P3HT presented superior charge extraction from the perovskite, and high charge transport, resulting in a champion solar cell PCE of 9.4% and improved operational stability. To enhance the stability and decrease the cost of the PSCs, we replaced the hole extraction layer and precious metal electrodes with a carbon electrode. We then used the device to build a monolithic photoanode with a NiFe catalyst layer for direct photo-driven oxygen evolution. To conclude, this thesis focused on improving the efficiency, stability, and cost-effectiveness of FAPbBr₃-PSCs. We achieved the targets by optimizing the fabrication process, passivating interfacial defects, and using alternative materials for the hole extraction layer and electrodes. The results suggest that the high bandgap FAPbBr₃ perovskite material shows promising applications in solar and photoelectrochemical cells.

Keywords: High-bandgap FAPbBr₃, additives, defect passivation, dopant-free HTMs, 2D perovskites, carbon electrode, oxygen evolution

Yawen Liu, Department of Chemistry - Ångström, Physical Chemistry, Box 523, Uppsala University, SE-75120 Uppsala, Sweden.

© Yawen Liu 2023

ISSN 1651-6214

ISBN 978-91-513-1810-3

URN urn:nbn:se:uu:diva-500172 (<http://urn.kb.se/resolve?urn=urn:nbn:se:uu:diva-500172>)

致我的家人和一直包容支持我的亲爱的朋友们

To people constantly supporting my research journey

To all Ph.D. students in struggling times

List of Papers

This thesis is based on the following papers, referred to in the text by their Roman numerals.

- I. **Liu, Y.**, Kim, B. J, Wu, H., Yuan, L., Zhu, H., Liu, A., Johansson, E. M. J. (2020) Flexible Lead Bromide Perovskite Solar Cells. *ACS Appl. Energy Mater.* 2020, 3 (10), 9817-9823.
- II. **Liu, Y.**, Cai, B., Yang, H., Boschloo, G., Johansson, E. M. J. Solvent Engineering of Perovskite Crystallization for High Performance FAPbBr₃ Perovskite Solar Cells Prepared in Ambient Condition. Submitted.
- III. **Liu, Y.**, Kim, B. J, Wu, H., Boschloo, G., Johansson, E. M. J. (2021) Efficient and Stable FAPbBr₃ Perovskite Solar Cells via Interface Modification by a Low-Dimensional Perovskite Layer. *ACS Appl. Energy Mater.* 2021, 4 (9), 9276-9282.
- IV. **Liu, Y.**, Cai, B., Johnson, C., Yang, H., Boschloo, G., Johansson, E. M. J. The Effects of Dopant-Free Hole Transport Materials on n-i-p FAPbBr₃ Perovskite Solar Cells under Ambient Processed. Manuscript.
- V. Yang, H., [†] **Liu, Y.**, [†] Ding, Y., Li, F., Wang, L., Cai, B., Zhang, F., Liu, T., Boschloo, G., Johansson, E. M. J., and Sun, L. Monolithic FAPbBr₃ Photoanode for Photoelectrochemical Water Oxidation with Ultralow-Onset-Potential. Submitted

Reprints were made with permission from the respective publishers.^{1,2}

Contribution

- Paper I

Planned and conducted the experimental work with Dr. Byeong Jo Kim. Fabricated solar cells, performed solar cell characterization, and prepared samples for most characterization techniques. Analyzed data and wrote the manuscript.

- Paper II

Carried out most of the experiments, analyzed data, and wrote the manuscript.

- Paper III

Planned and conducted the experimental work with Dr. Byeong Jo Kim. Fabricated solar cells, performed solar cell characterizations, and prepared samples for most characterization techniques. Analyzed data and wrote the manuscript.

- Paper IV

Carried out most of the experiments and characterizations, analyzed data, and wrote the manuscript. Catherine Johnson assisted in the laser spectroscopy part, including measurement, manuscript writing, and data analysis.

- Paper V

Carried out all solar cells experiments and characterization and analyzed data. Hao Yang performed all the experiments on the catalyst part and analyzed the data. We wrote the manuscript together.

Extended bibliography

I have contributed to the following publications during my time in postgraduate studies, but they are not included in this thesis.

1. X. Geng, **Y. Liu**, X. Zou, E. M. J. Johansson, and J. Sá Transient Energy-Resolved Photoluminescence Study of Excitons and Free Carriers on FAPbBr₃ and FAPbBr₃/SnO₂ Interfaces *The Journal of Physical Chemistry C* 2023 127 (6), 3085-3092
2. X. Zou, R. B. Vadell, **Y. Liu**, A. Mendalz, M. Drillet, and J. Sá Photophysical Study of Electron and Hole Trapping in TiO₂ and TiO₂/Au Nanoparticles through a Selective Electron Injection. *The Journal of Physical Chemistry C* 2022 126 (50), 21467-21475
3. H. Cheng, **Y. Liu**, B. Cai, C. Hägglund, T. Kubart, G. Boschloo, and H. Tian Atomic Layer Deposition of SnO₂ as an Electron Transport Material for Solid-State P-type Dye-Sensitized Solar Cells. *ACS Applied Energy Materials* 2022 5 (10), 12022-12028
4. H. Yang, F. Li, S. Zhan, **Y. Liu**, W. Li, Q. Meng, A. Kravchenko, T. Liu, Y. Yang, Y. Fang, L. Wang, J. Guan, I. Furó, M. S. G. Ahlquist, L. Sun. Intramolecular Hydroxyl Nucleophilic Attack Pathway by a Polymeric Water Oxidation Catalyst with Single Cobalt Sites. *Nature Catalysis* 2022, **5**, 414-429.
5. H. Wu, Y. Wang, A. Liu, J. Wang, B. J. Kim, **Y. Liu**, Y. Fang, X. Zhang, G. Boschloo, E. M. J. Johansson, Methylammonium Bromide Assisted Crystallization for Enhanced Lead-Free Double Perovskite Photovoltaic Performance. *Adv. Funct. Mater.* 2022, 32, 2109402.
6. A. Liu, S. Wang, H. Song, **Y. Liu**, L. Gedda, K. Edwards, L. Hammarström and H. Tian Excited-state and charge-carrier dynamics in binary conjugated polymer dots towards efficient photocatalytic hydrogen evolution *Phys. Chem. Chem. Phys.*, 2023, **25**, 2935.

Contents

| | |
|---|----|
| Introduction..... | 13 |
| Solar Cells | 13 |
| Solar Cell Working Mechanism | 13 |
| Silicon Solar Cells | 15 |
| Thin Film Solar Cells..... | 16 |
| Perovskite Solar Cells..... | 16 |
| Fabrication methods of PSCs..... | 19 |
| Structure of PSCs..... | 22 |
| Optimization methods of PSCs..... | 23 |
| Emerging high bandgap PSCs | 24 |
| Aims of this Thesis..... | 25 |
| Experimental..... | 26 |
| Device fabrication | 26 |
| Characterization Techniques | 26 |
| Characterization of PSCs | 30 |
| Results and discussion | 34 |
| Perovskite crystal growth control by the additives and solvent engineering | 34 |
| Passivation of the defects on the perovskite by 2D perovskite | 42 |
| Acceleration of hole extraction by using dopant-free hole transport materials | 47 |
| Integration of carbon electrode and FAPbBr ₃ for photovoltaic and photoelectrochemical application..... | 52 |
| Conclusions and Outlook..... | 69 |
| Acknowledgments..... | 72 |
| Popular science summary | 75 |
| Populärvetenskaplig sammanfattning | 78 |
| Reference | 81 |

Abbreviations

| | |
|---|---|
| β | Exciton concentration |
| θ | Angle λ wavelength |
| σ | Conductivity |
| φ | Photon flux |
| μ | Charge mobility |
| A | Area |
| AM1.5G | Air mass 1.5 global |
| Ag | Silver |
| ΔA | Light absorption difference |
| α -Si | Amorphous silicon |
| Au | Gold |
| ATR | Attenuated total reflectance |
| A_λ | Absorptance c speed of light |
| CB | Conduction band |
| CE | Counter electrode |
| $\text{CH}_3\text{NH}_3\text{PbI}_3/\text{MAPI}/\text{MAPbI}_3$ | Methylammonium lead iodide |
| DMF | N, N-dimethylformamide |
| DMSO | Dimethyl sulfoxide |
| ESL | Electron selective layer |
| ETL | Electron transport layer |
| E_g | Energy band gap |
| FAPbBr ₃ | Formamidinium lead bromide |
| FF | Fill factor |
| FTIR | Fourier transform infrared spectroscopy |

| | |
|---------------------|--|
| FTO | Fluorine-doped tin oxide |
| h^+ | Hole |
| HOMO | Highest occupied molecular orbital |
| HTM | Hole transport material |
| HTL | Hole transport layer |
| I | Current |
| I | Iodine |
| IPA | Isopropanol |
| IPCE | Incident photon to collected electron efficiency |
| ITO | Indium tin oxide |
| J | Current density |
| J_{sc} | Short circuit current density |
| k | Rate constant |
| l | Length |
| LUMO | Lowest unoccupied molecular orbital |
| MA | Methylammonium |
| MeOH | Methanol |
| MPP | Maximum power point |
| mp TiO ₂ | Mesoporous TiO ₂ |
| M | Molar (mol per liter) |
| n | Electron concentration |
| OPV | Organic photovoltaic |
| P | Power |
| p | Hole concentration |
| P3HT | Poly(3-hexylthiophene-2,5-diyl) |
| PbBr ₂ | Lead bromide |
| PCE | Power conversion efficiency |
| PTB7 | Poly[[4,8-bis[(2-ethylhexyl)oxy]benzo[1,2-b:4,5-b']dithiophene-2,6-diyl][3-fluoro-2-[(2- |

| | |
|---------------------|---|
| | ethylhexyl)carbonyl]thieno[3,4-b]thiophenediyl]] |
| PSC | Perovskite solar cell |
| PCBM | [6,6]-Phenyl-C61-butyric acid methyl ester |
| PDMS | Polydimethylsiloxane |
| PEN | Polyethylene Naphthalate |
| PL | Photoluminescence |
| r | Effective ionic radius |
| rpm | Rotations per minute |
| R | Resistance |
| R_{series} | Series resistance |
| R_{shunt} | Shunt resistance |
| R | Reflectance |
| RHE | Reversible Hydrogen Electrode |
| SE | Secondary electron |
| SEM | Scanning electron microscopy |
| SiSC | Silicon solar cell |
| Spiro-OMeTAD | 2,2',7,7'-Tetrakis[N,N-di(4-methoxyphenyl)amino]-9,9'-spirobifluorene |
| t | Tolerance factor |
| T_{λ} | Transmittance |
| TQ1 | Poly((2,3-bis(3-octyloxyphenyl)-5,8-quinoxalinediyl)-2,5-thiophenediyl) |
| V | Voltage |
| VB | Valence band |
| V_{oc} | Open circuit voltage |
| XRD | X-ray diffraction |
| XPS | X-ray photoelectron spectroscopy |

Introduction

Energy plays a crucial role in the advancement of human civilization. As society continues to evolve, new energy sources are being discovered and utilized, leading to a gradual phase-out of older energy sources. At the end of the 19th century, the world entered the "coal age," with the extensive use of coal playing a significant role in boosting industrial growth and the pace of social modernization. In the 1960s, oil and natural gas exploration and usage led to decreased coal usage and marked the start of the "oil age." While fossil fuels such as coal and oil have positively impacted society, the energy crisis and environmental issues caused by combustion and CO₂ emission have become increasingly important.

As a result, the development of renewable and environmentally friendly energy sources such as hydro, wind, solar, biomass, geothermal, and tidal energy has become increasingly critical. Among these sources, solar energy is the most abundant, accessible, and cleanest form of energy on Earth, with the amount of energy reaching the Earth's surface each year equating to the energy released by 130 trillion tons of coal. It is also easily accessible, making it a vital component of sustainable development.

Therefore, solar energy is poised to play a significant role as a future energy source for humanity, and the research and development of low-cost, high-efficiency solar cells have become a major focus in recent years.

Solar Cells

Solar Cell Working Mechanism

The photovoltaic effect refers to the phenomenon where light causes a potential difference between different parts of an inhomogeneous semiconductor or between a semiconductor and a contact material. A potential difference is generated at a semiconductor p-n junction or semiconductor/contact material interface due to a difference in quasi-Fermi energies of electrons and holes.

In 1839, Edmond Becquerel observed the fundamental principle behind solar cells: when exposed to light, the solar cell creates a potential difference

between two electrodes.³ A typical solar cell device includes a photo-absorber and two selective contacts. The separation of photogenerated charges at opposite electrodes results in photovoltage. This separation can be achieved by creating an electric field within the material of the solar cell that causes electrons to move in one direction and holes (positive charges) to move in the opposite direction. For example, a p-n junction can be constructed by doping one part of a silicon semiconductor with elements resulting in a mobile positive charge (p-type) and another with elements resulting in a mobile negative charge (n-type). When these two pieces are joined, a p-n junction is formed, and the difference in charge concentration creates an electric field in the depletion region.

The separation of charges generates a current, which can produce electrical power when connected to an external circuit. The potential difference between the electrodes that is obtained during the illumination of light gives a voltage, which, together with the current, results in electrical power.

When the semiconductor absorbs a photon, it excites an electron from the VB to the CB, forming an electron-hole pair (e^-h^+) with a hole remaining in the VB. Typically, the electron-selective layer, known as an n-type semiconductor material, usually has higher electron mobility and lower hole mobility. On the other hand, the hole-selective layer refers to a p-type semiconductor material that exhibits a comparatively high hole mobility, allowing for efficient hole transport. The energy level gradient formed between the various materials within the device and the built-in electric field, along with the relatively high energy barrier for electrons injected into the hole transport layer (HTL) and the high potential barrier for holes injected into the electron transport layer (ETL), ensures that electrons and holes follow their respective transmission paths into the external circuit. The working mechanism of solar cells is shown in **Figure 1-1**.

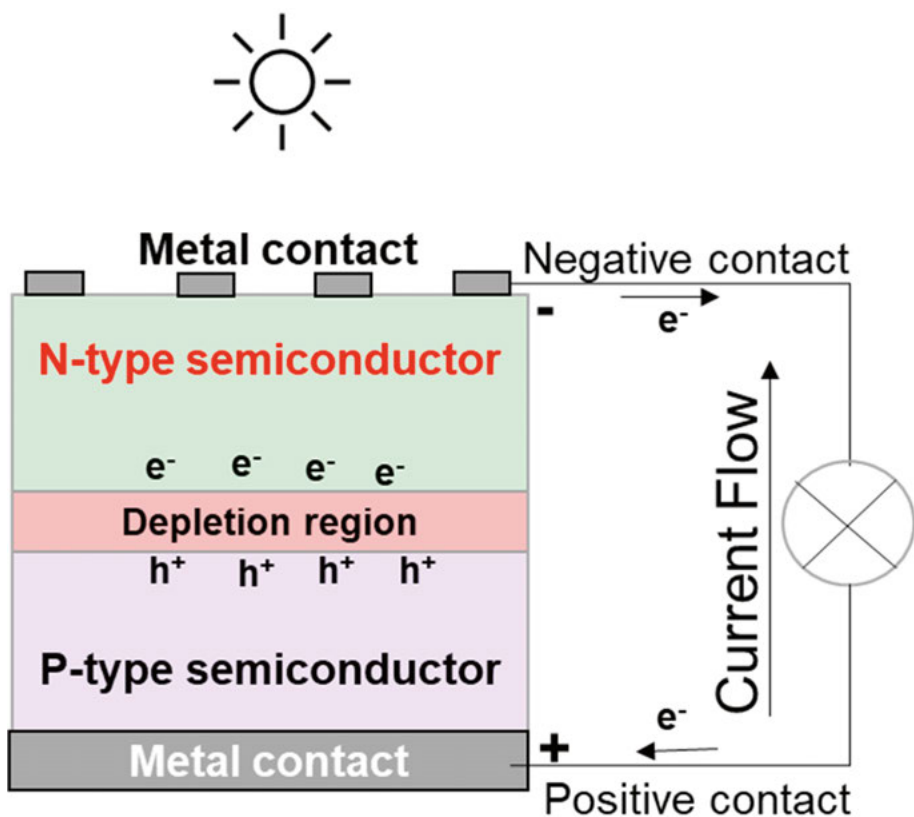


Figure 1-1 Solar cell working mechanism.

Silicon Solar Cells

Silicon solar cells currently dominate the photovoltaic market, categorized as the first generation of photovoltaic technology.⁴ The dominance of silicon solar cells in the photovoltaic market is mainly attributed to their high PCE and long lifetime. There are two primary types of silicon solar cells: monocrystalline and polycrystalline. Monocrystalline cells are constructed using single silicon crystals sliced into uniform, continuous, and non-broken pieces after being derived from large pure silicon crystals. However, the growth of the large crystals requires stringent and expensive processing conditions and their PCE decrease when temperatures exceed 25°C.⁵ Polycrystalline cells comprise numerous small crystals that can be seen on the surface of the polycrystalline solar panels. The size of these grains limits the PCE of the cells, and smaller grain sizes lead to increased grain boundaries and recombination. Like monocrystalline silicon solar cells, the PCE of polycrystalline cells also declines beyond 25°C temperatures. The best-recorded laboratory PCE for

monocrystalline cells (27.6%) is higher than that of polycrystalline cells (23.3%).⁶

Thin Film Solar Cells

Thin film solar cells are considered the second generation of photovoltaics. Unlike traditional silicon solar cells, the photovoltaic layer in thin film solar cells is much thinner, from around several nanometres to several microns, compared to the 160-190 microns thickness of a silicon wafer. These solar cells are created by depositing thin layers of photovoltaic materials, such as GaAs, InP, CIGS, CdTe, etc.⁷ Thin film solar cells have the advantages of high PCE, flexibility, and stable performance at high temperatures. This makes them an attractive option in the solar energy industry, and they are expected to expand the application of solar cells, *e.g.*, in space. Thin film solar cells are stable at high temperatures, can be prepared into flexible devices, and can be mass-produced. However, using toxic and rare elements in the materials poses a challenge to their large-scale adoption. Besides, many other emerging solar cells are considered the third generation of photovoltaics, such as organic photovoltaic cells, dye-sensitized solar cells, PSCs, etc. Among them, PSCs show one of the most outperformed PCE, and our thesis relates to it.⁶

Perovskite Solar Cells

The perovskite mineral was named after Lev Perovski in the 19th century, and the crystal structure of perovskite with the form ABX_3 was initially explored by Victor Goldschmidt, who studied this family of minerals.⁸ **Figure 1-2** shows that A represents a cation, B denotes a metal cation, and X signifies an anion. For most popular materials of the inorganic and organic hybrid metal halide perovskites solar cells, A = $CH_3NH_3^+$ (MA), $CH(NH_2)_2^+$ (FA), Cs^+ , etc.; B = Pb^{2+} , Sn^{2+} , Ti^{4+} , Bi^{3+} , etc.; X = Cl^- , Br^- , I^- , etc.⁹⁻¹² D. Weber synthesized the methylammonium lead triiodide ($MAPbI_3$) in 1978^{13, 14} and discovered that this specific subclass of perovskite materials could have photoactive properties. Then Kojima *et al.* fabricated the first hybrid organic-inorganic perovskite solar cell using $MAPbI_3$ as the photo absorber in 2009.¹⁰ The development of PSCs was very rapid, and the PCE has increased to 25.7% for single junction devices as shown in **Figure 1-3**.^{9, 10, 15, 16} The PSC working principle is similar with other solar cells and the band diagram of PSCs solar cells is shown in **Figure 1-4**.

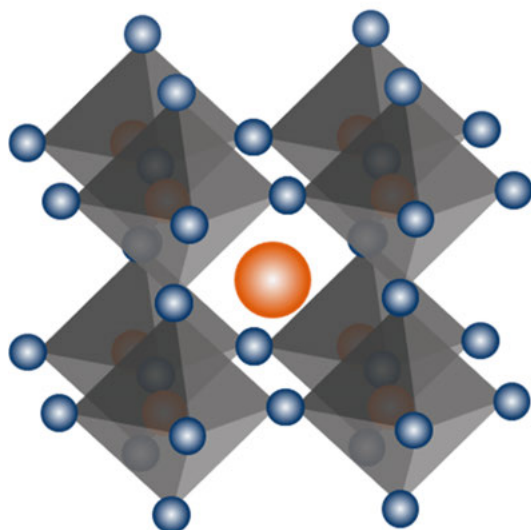


Figure 1-2 The structure of an ABX_3 type perovskite.

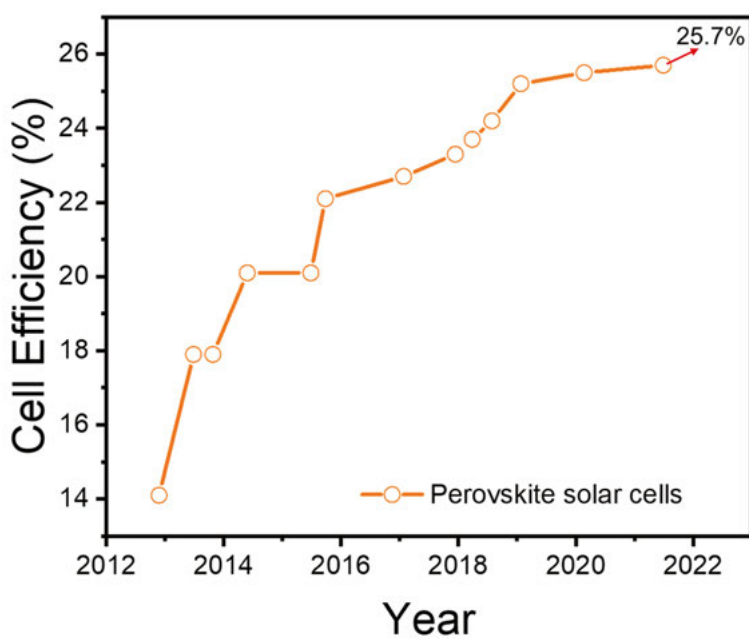


Figure 1-3 The chart of the development best research efficiency of PSCs.
Source: NREL.⁶

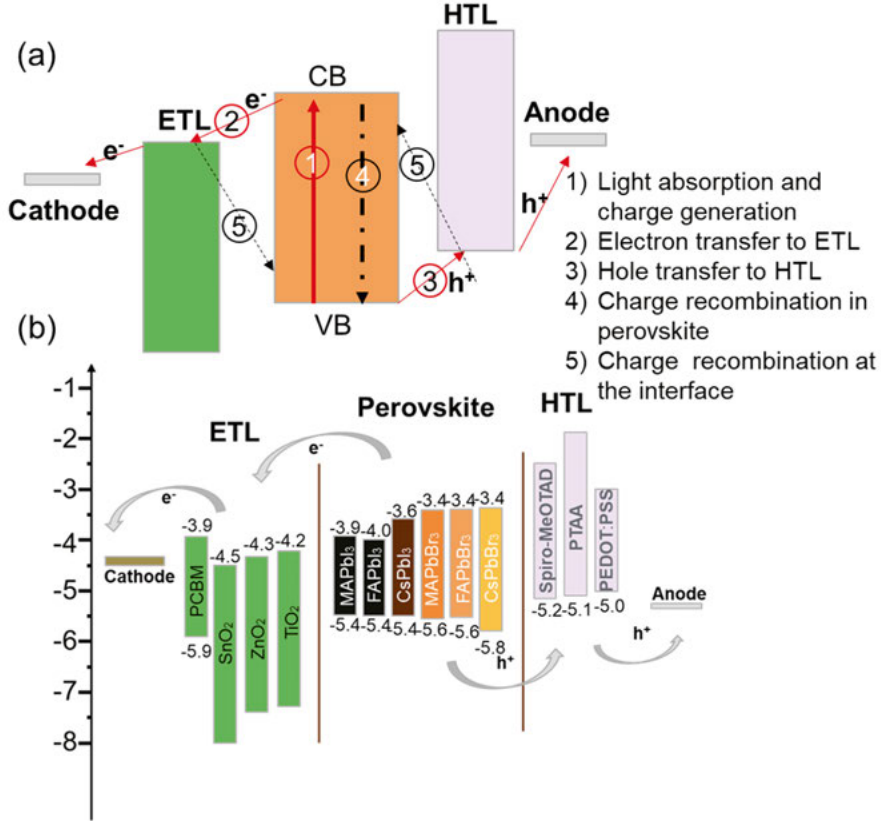


Figure 1-4 (a) Schematic figure of the working mechanism of PSCs and (b) energy bands of the materials in PSC solar cells.¹⁷⁻¹⁹

In the early 20th century, as the understanding of perovskite deepened, researchers became increasingly interested in exploring and developing the crystal structure theory of this material. A concept known as the "tolerance factor" (t) was introduced to measure the stability of the perovskite structure. This parameter quantifies the relationship between the structural stability and the composition of the perovskite material.⁸

At the inception of PSCs research, several organic-inorganic perovskite crystal structures were discovered to have photoactive properties, but their potential as solar cell materials had not yet been fully explored.²⁰ By comparing the relative sizes of the ions, t can indicate whether a specific combination of the ABX₃ ions can form a perovskite. The equation for t is:

$$t = \frac{r_A + r_X}{\sqrt{2}(r_B + r_X)} \quad (1)$$

Where r_A , r_B , and r_X are the radii of the A-cation, B-cation, and X-anion, respectively. Shannon's crystal ionic radii are used to determine the ionic radii of inorganic ions. At the same time, the values are computed using discrete Fourier transform for organic cations.^{21, 22} Research and experience indicate that the tolerance factor of structurally stable perovskite compounds is typically between 0.78~1.05.²³ When t is 0.9~1.0, indicates the presence of an ideal cubic perovskite structure. If t deviates more from 1.0, other low-symmetry structures will usually be formed.²¹ Moreover, even though t is within the range for cubic structure, the framework of perovskite can distort under high temperature and pressure, which will influence the photovoltaic properties of perovskites.²⁴

Fabrication methods of PSCs

The preparation methods of the organic-inorganic perovskite light-absorbing layer are crucial for PSCs' performance. A high-quality perovskite film should be crystalline, smooth, and dense, promoting the generation and separation of photogenerated carriers within the bulk. On the contrary, a rough film with obvious pores decreases the photovoltage and photogenerated current, provides a recombination path by making contact between the ETL and HTL, decreases the parallel resistance of the device, and forms trap states as recombination centers for carriers. Currently, the organic-inorganic perovskite composite film preparation methods include one-step spin coating, two-step method (stepwise liquid immersion and spin coating), co-evaporation and stepwise gas-assisted deposition, *etc.* These methods will be shown below.

One-step method:

As shown in **Figure 1-5**, the one-step method uses a precursor solution by mixing a certain proportion of BX_2 with AX ($A = MA, FA, Cs^+$, etc.; $B = Pb^{2+}, Sn^{2+}, Ti^{4+}, Bi^{3+}$, etc.; $X = Cl^-, Br^-, I^-$, etc.) and form a perovskite film by spin-coating followed by annealing. The annealing temperature depends on the perovskite components to ensure solvent evaporation and promote crystal formation. The one-step deposition is usually assisted by drop-casting the anti-solvent to control solvent evaporation and polycrystalline perovskite crystallization. The perovskite film prepared through this approach is very sensitive to the conditions, such as the solvent and concentration of the precursor solution, the annealing temperature, the timing for anti-solvent casting, *etc.*²⁵⁻²⁷

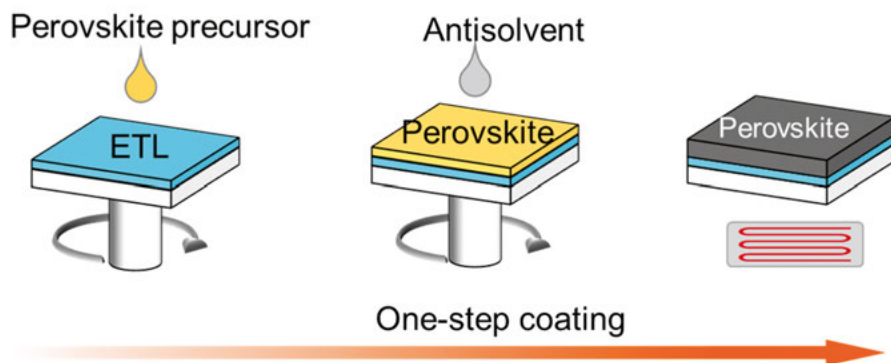


Figure 1-5 One-step coating method process.

Two-step method:

Figure 1-6 shows that the two-step method includes spin-coating the BX_2 film and then spin-coating a suitable amount of AX film to form a double-layer film. The mutual diffusion and reaction between the two layers are achieved through annealing, generating a single-component organic-inorganic perovskite film. For example, its formation mechanism is that the intermediate ($PbI_2 \cdot DMF$) consists of a relatively weak coordination bond between Pb and DMF . When MAI is spin-coated, with DMF volatilizing, $PbI_2 \cdot DMF$ reacts with MAI to form perovskite.²⁸ The alternative approach is dip-coating: The second step then involves the immersion of a BX_2 (such as PbI_2) film into an AX solution (such as MAI), which leads to the transformation into an organic-inorganic perovskite.

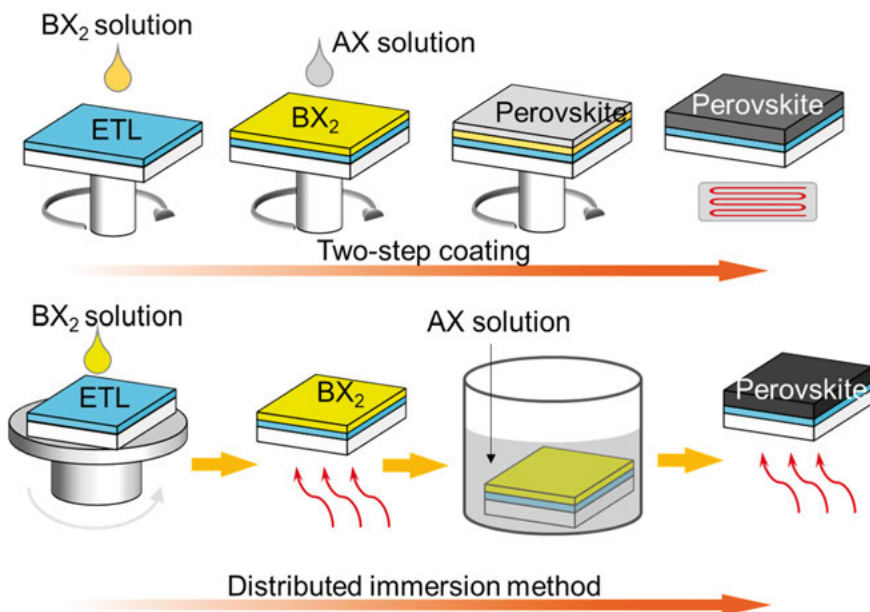


Figure 1-6 Two-step method process.

Vapor deposition:

The vapor deposition method process is shown in **Figure 1-7**. The technique of preparing PSCs by gas phase deposition was first reported by Snaith et al.²⁶ The film surface prepared by gas phase deposition is smooth, dense, and uniform in thickness. This makes the evaporation methods promising in large-scale deposition and tandem cell fabrication.

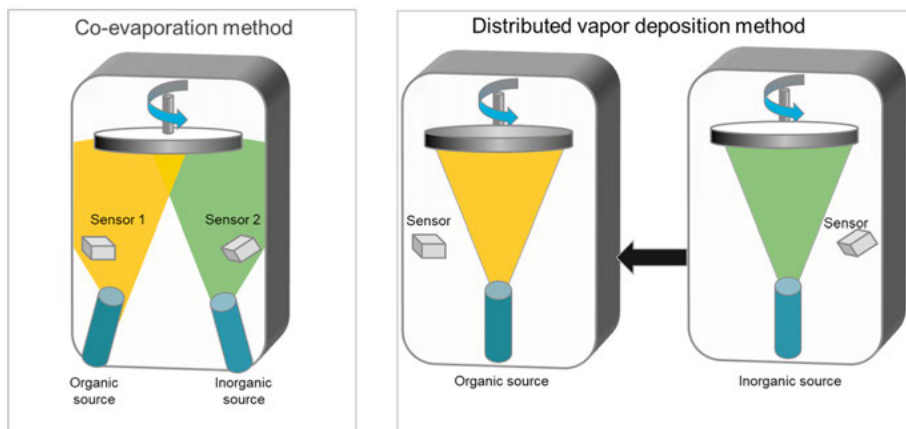


Figure 1-7 Vapor deposition method process.

Structure of PSCs

The main structures of perovskite solar cell devices include mesoporous structures, standard planar structures, inverted planar structures, ETL-free structures, HTL-free structures, and carbon electrode structures. **Figure 1-8** illustrates several typical structures of PSCs. The most commonly used structures are mesoporous structures and planar structures.

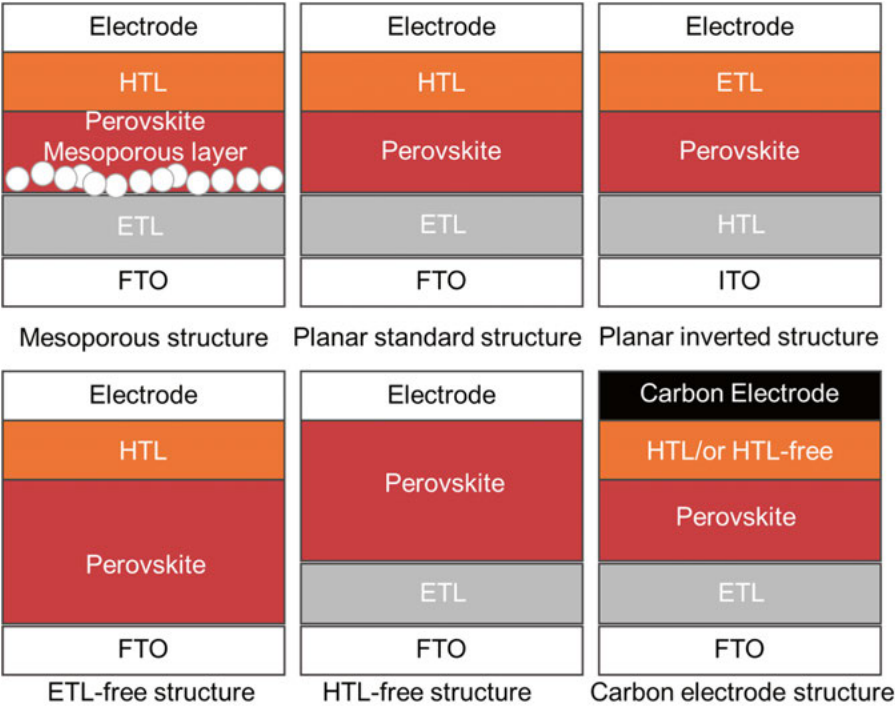


Figure 1-8 Different structures of PSCs.

Mesoporous structures

The mesoporous structure mainly consists of several layers, including a conducting glass (FTO), an electron-blocking layer, a mesoporous layer, a perovskite light-absorbing layer, an HTL, and an electrode. The mesoporous layer is typically made of materials such as TiO_2 and plays a pivotal role in supporting the perovskite material and improving the film quality. The mesoporous structure can also increase light absorption and reduce the recombination of holes and electrons, improving the solar cell's efficiency. The mesoporous layer can be made of materials such as TiO_2 ,²⁹ ZnO ,³⁰ to help with film formation and conduct charge transfer. One advantage of the mesoporous

structure is the shorter diffusion length for the electrons to the ETL, leading to increased efficiency. However, the thickness of the mesoporous layer may reduce the efficiency of charge carrier collection. Preparing the mesoporous layer also requires high-temperature sintering, making production of large-scale or flexible devices difficult.

Planar structures

Planar-structured PSCs do not use mesoporous skeletons compared to mesoporous structure devices. This avoids some restrictions on solar cell preparation technology imposed by mesoporous skeletons, simplifies the solar cell structure, greatly expands the application of PSCs in terms of material systems and preparation technology, and helps to achieve applications of PSCs in functional devices through an improvement in flexibility. Therefore, compared to mesoporous structured PSCs, the later-developed planar structured PSCs have received more extensive research. Planar structure solar cells are divided into the standard structure (n-i-p) and inverted structure (p-i-n). In a device with a standard structure, light enters in the order of ETL, then perovskite layer, and finally HTL, while the order of light penetration is reversed in a device with an inverted structure. The conventional electron and hole transport materials in standard structure devices are TiO_2 or SnO_2 and Spiro-OMeTAD, respectively. With SnO_2 as ETL, the planar PSCs yielded a record PCE of 25.7%.³¹ For the inverted structure PSCs, the common HTLs are PEDOT: PSS, PTAA, and nickel oxide, and the common ETL are PCBM.

In this thesis, we applied the SnO_2 -based standard planar structure, which is the optimized structure, to fabricate our high bandgap devices.

Optimization methods of PSCs

As mentioned previously, the tolerance factor (t) is a highly important theoretical parameter for predicting the stability of perovskite crystal structures. Despite this, in practical applications, the stability of common hybrid perovskites is often poor when exposed to water, light, or oxygen. Research has focused on developing methods for creating high-stability devices to enhance the commercial potential of solar cells. The key to success is ensuring the high quality of the perovskite material. One approach that has shown promising results is the addition of additives like methylammonium bromide (MABr) and methylammonium chloride (MACl), which can assist the growth of perovskite crystals and significantly enhance the quality of the perovskite films.^{11, 32} Specifically, the performance of a device is significantly impacted by defects, such as interfacial defects. These defects can result in notable hysteresis in the current density–voltage curves (J - V) characteristics due to ion migration and degradation in the device's lifetime due to moisture accumulation at these

defect sites.^{33-35 34, 36-38} Layering a more stable 2D perovskite on the surface of the 3D perovskite can aid in enhancing solar cell stability. This technique effectively engineers the interface, leading to improved stability overall.^{39, 40} Doped HTMs with high conductivities are necessary for high device power conversion efficiencies.⁴¹ At the same time, the moisture-absorbing dopants would cause stability problems and degradation of the devices due to the ion immigration and the hydrophilic nature of ionic additives.⁴²⁻⁴⁶ Therefore, the design of different dopant-free hole-transport materials into PSCs enhanced the stability of PSCs.^{47, 48} To address these limitations, researchers have tried eliminating HTLs from conventional n-i-p structured PSCs, given the ambipolar nature of perovskite materials as both light harvesters and HTLs.⁴⁹ Carbon electrodes have emerged as a viable alternative for HTL-free PSCs, owing to their robust stability via moisture barrier properties and inhibited ion migration.⁵⁰ Carbon has been selected as a hole extraction electrode for PSCs due to its economic viability, capacity to resist ion migration and water, and favorable energy bandgap alignment with most perovskites. Additionally, carbon allows for simpler and more accessible fabrication techniques, such as doctor-blade or screen-printing methods, in contrast to the high vacuum evaporation requirements of metal electrodes.

Emerging high bandgap PSCs

While high PCE is a crucial aspect of solar cells, high photovoltage has also gained attention due to its importance in top cells of tandem solar cells and light-assisted water splitting.⁵¹⁻⁵⁸ In recent years, bromide PSCs with a high bandgap that result in high open-circuit voltage (V_{oc}) have gained popularity. The larger size of the iodide ion leads to a smaller lattice constant and a larger overlap between the valence band (VB) and conduction band (CB), resulting in a smaller bandgap energy. This is why MAPbI₃ has a smaller bandgap energy than MAPbBr₃. However, in terms of stability, bromide perovskite is more stable than other perovskite materials, including MAPbI₃. This is because the iodide ion is more prone to oxidation than the bromide ion, which can lead to the formation of defects and the degradation of the perovskite material over time. These bromide PSCs also exhibit excellent stability in humidity and oxygen in ambient air.^{56, 59} Bromide perovskites exhibit a bandgap range of 2.2-2.4 eV and have a Shockley–Queisser efficiency limit of approximately 15%, and they also have a high ceiling for visible transparency.⁶⁰ Notably, bromide perovskites that consist of a single A-site cation, such as MA, FA, and cesium, exhibit superior stability in the photoactive phase compared to iodide perovskites.⁶¹ Here, we selected FAPbBr₃ perovskite as an absorber due to several merits of this material. The larger ionic radius of FA⁺ compared to MA⁺ results in a larger lattice constant for FAPbBr₃ than MAPbBr₃, leading

to improved structural and thermal stability.^{62, 63} Indeed, when exposed to heat and moisture, MAPbX₃ undergoes decomposition into gaseous methylamine and hydrogen iodide, which can lead to a loss of optical extinction coefficient and several instances of charge carrier recombination.⁶⁴ In contrast to CsPbBr₃, which typically requires high temperatures and poses challenges in controlling phase purity, the synthesis of FAPbBr₃ is expected to be relatively easier.⁶⁵ Moreover, Zhumekenov et al. reported an exceptionally long carrier diffusion length of 19 μm for FAPbBr₃ crystals,⁶⁶ of which are among the largest reported values in halide perovskite materials.

There have been several reports on FAPbBr₃ thus far.^{62, 67} Hanusch et al. were the first to report on FAPbBr₃-PSCs with an efficiency of 6.5 %.⁶⁸ Arora et al.⁵⁹ later improved on this by using FAPbBr₃ as a light absorber in a regular mesoscopic-TiO₂ cell structure, achieving an efficiency of 8.2% through interface engineering and minimal hysteresis. Due to its high electron mobility and low photocatalytic activity, SnO₂ is considered a competitive ETL material that holds the potential to enhance the efficiency and stability of solar cells.^{69, 70} As reported by Zhang et al.⁵³, the incorporation of urea as an additive in SnO₂-based FAPbBr₃ has been demonstrated.

Aims of this Thesis

As noted in the introduction, research on solar cells is essential for transitioning to renewable energy sources. High-band gap perovskites, *e.g.*, FAPbBr₃, have great potential in tandem devices, solar water splitting, and CO₂ reduction devices.⁵¹⁻⁵⁸ But many things are still unclear regarding the preparation, properties, and application of FAPbBr₃. This thesis aims to understand and improve the preparation of high bandgap FAPbBr₃ and to achieve high efficiency, excellent stability, and ease of fabrication of FAPbBr₃ solar cells. Furthermore, we also succeeded in using FAPbBr₃ as a photoanode in solar water splitting and achieved remarkable results.

Experimental

Device fabrication

The structure of PSCs in this thesis is almost the same, and more specific details about the materials and components will be provided in the relevant chapters. Typically, the perovskite films were prepared using a two-step spin-coating process. The FTO or ITO glasses were ultrasonically cleaned with detergent, acetone, isopropanol (IPA), and water, followed by a 30-minute UV/ozone (UVO) treatment. The structure of the PSCs is as follows: Glass/FTO (or ITO)/ETL (SnO_2)/perovskite/HTL/Au. The SnO_2 film was deposited on the FTO or ITO substrate by spin-coating a commercial SnO_2 colloidal solution and annealing in air. Then, the substrate underwent a 20-minute UV/ozone treatment before use. The fabrication of the PSCs involved the following steps: dissolution of PbBr_2 in a mixture of DMF and DMSO to create a precursor solution, spin-coating of the precursor solution onto SnO_2 substrates, depositing the FAPbBr₃ solution on the surface of the PbBr_2 precursor films and annealing. The HTM solution was spin-coated onto the perovskite film, and the conductive electrode was deposited on top of the HTL layer. The PSCs were stored in a dry box overnight before the J - V measurement.

Characterization Techniques

The perovskite films and devices were characterized using various techniques, which are briefly described below. Certain characterization methods used in specific papers that were analyzed are not included in this list.

UV-vis Spectroscopy

UV-vis spectroscopy (UV-Vis) involves recording absorption signals due to electronic transitions. In semiconductors, absorption occurs when the incident photon energy exceeds the band gap energy of the materials, and the spectrometer records the signal (the transmitted photons). In this thesis, UV-Vis spectra were recorded with an HR-2000 Ocean Optics spectrophotometer with baseline correction. Light absorption in the wavelength range of 200 to 1100 nm was performed to assess the overall absorption properties of thin films. UV-Vis refers to absorption or reflectance spectroscopy in part of the

ultraviolet and visible regions of the electromagnetic spectrum. Due to its low cost and simple implementation, this technique is extensively utilized in various practical and fundamental applications.

Photoluminescence Spectroscopy

When a semiconducting material absorbs a photon, an e^- is excited from the VB to the CB of the material. Unless the charge is extracted through a circuit, the excited photo absorber has two possible mechanisms for recombination to its ground state, nonradiative or radiative. Radiative recombination entails that the material emits a photon of energy corresponding to its E_g . A strong photoluminescence (PL) emanating from a photo absorber is highly desirable as it implies the presence of minimal nonradiative recombination pathways within the material, such as surface defects. This observation, therefore, suggests great material quality. The photoluminescence of a material can be monitored by typically illuminating a sample with monochromatic light of higher energy than its band gap energy and then using a second monochromator placed perpendicularly to the incident illumination to collect and analyse, the emission spectrum of the sample.

In this thesis, steady-state photoluminescence (SSPL) and time-resolved photoluminescence (TRPL) were obtained by a PL spectrometer (Edinburgh Instruments, FLS 980, UK). The traces obtained from TRPL are typically fitted using the equation: $y = y_0 + A_1 \exp(-(x-x_0)/\tau_1) + A_2 \exp(-(x-x_0)/\tau_2)$, where τ_1 and τ_2 represent fast and slow decay time constants, respectively.⁷¹ The τ_1 is usually related to trap-induced nonradiative recombination and τ_2 with radiative recombination.⁷² The equation calculates the average decay time constant (τ_{ave}): $\tau_{ave} = \tau_1 A_1 / (A_1 + A_2) + \tau_2 A_2 / (A_1 + A_2)$.⁷¹

X-Ray Diffraction

The X-ray diffraction (XRD) technique is widely used to determine the structural properties of materials, such as crystal structure, lattice parameters, crystallite size, and orientation. The working principle of XRD is shown in **Figure 2-1**. When an incident X-ray beam encounters a lattice of atoms within a crystalline film, it undergoes partial reflection. Specifically, when the incident beam intersects the material at an angle θ with an inter-planar distance of d , the beam reflected by the second layer of atoms travels an additional distance of $2d \sin \theta$. Constructive interference occurs when the incident electromagnetic waves have a wavelength λ and satisfy the equation $2d \sin \theta = n\lambda$, where n is an integer-called order of diffraction. This is known as the Bragg condition. A diffraction pattern can be collected by measuring the intensity of the diffraction signal obtained for different angles θ . Peaks appear in the XRD pattern when the scattering angle satisfies the Bragg condition. The XRD

analyses conducted for this thesis utilized a Siemens D5000 θ - 2θ equipped with a 0.4° Soller slit collimator and Cu K α ($\lambda = 1.54051 \text{ \AA}$) radiation. The instrument had a resolution of $2\theta = 0.3^\circ$ (Bruker AXS, Karlsruhe, Germany) and was operated at room temperature. This measurement was compared to previously reported data to confirm the perovskite crystal structures.

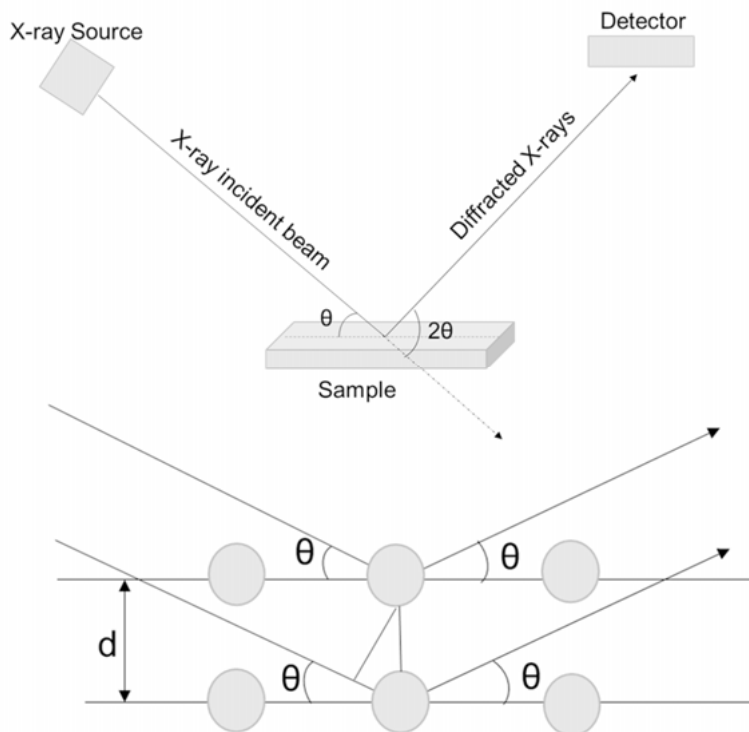


Figure 2-1 The working principle of XRD.

X-Ray Photoelectron Spectroscopy

The X-ray photoelectron spectroscopy (XPS) was measured using a PHI Quantera II from Physical Electronics. This technique was employed to evaluate the composition of the perovskite films, specifically the relative amounts of elements present. The samples were fixed in the sample chamber, which was then evacuated. The electrons were excited by an Al K α source and emitted from the sample, ultimately reaching the detector. From the resulting element-specific signals, the atomic ratios of each element in the perovskite film were calculated by integrating the area under the background-corrected and fitted peaks and using the appropriate relative sensitivity factors for each element to determine the correct relative areas.

Fourier Transform Infrared Spectroscopy

Fourier transform spectroscopy (FTIR) differs from traditional spectroscopy in collecting the spectrum. In FTIR, a broad-spectrum light source illuminates the sample, and the information about the sample's spectrum is measured using a Michelson interferometer. This information can then be extracted from the interferogram using Fourier transform. ATR (attenuated total reflectance) sampling is a commonly used method in FTIR for measuring solid thin films or liquids. During ATR sampling, IR light undergoes internal reflection at the crystal-sample interface after passing through a crystal. This produces an evanescent wave when a portion of the IR light enters and is absorbed by the sample. The refractive index difference between the sample and the ATR crystal determines the penetration depth of the evanescent wave into the sample. ATR sensors with different refractive indices can suit different sample types and path length requirements. In this thesis, IR spectra were obtained using a Bruker Vertex 70v Fourier transform infrared spectrometer in ATR mode.

Scanning Electron Microscopy

To visualize the surface morphology and cross-sectional thickness of solar cell devices, Scanning Electron Microscopy (SEM) was utilized. The sample was bombarded with a high-power electron beam emitted from an electron gun, and a secondary electron detector was used to capture an image of the sample. The interaction between the electrons and the materials in the sample caused variations in contrast, which were visible in the resulting image. Our SEM images were taken by ZeissLEO1530/1550 microscopes with beam accelerator voltages: of 3 or 5 kV, as shown in **Figure 2-2**.

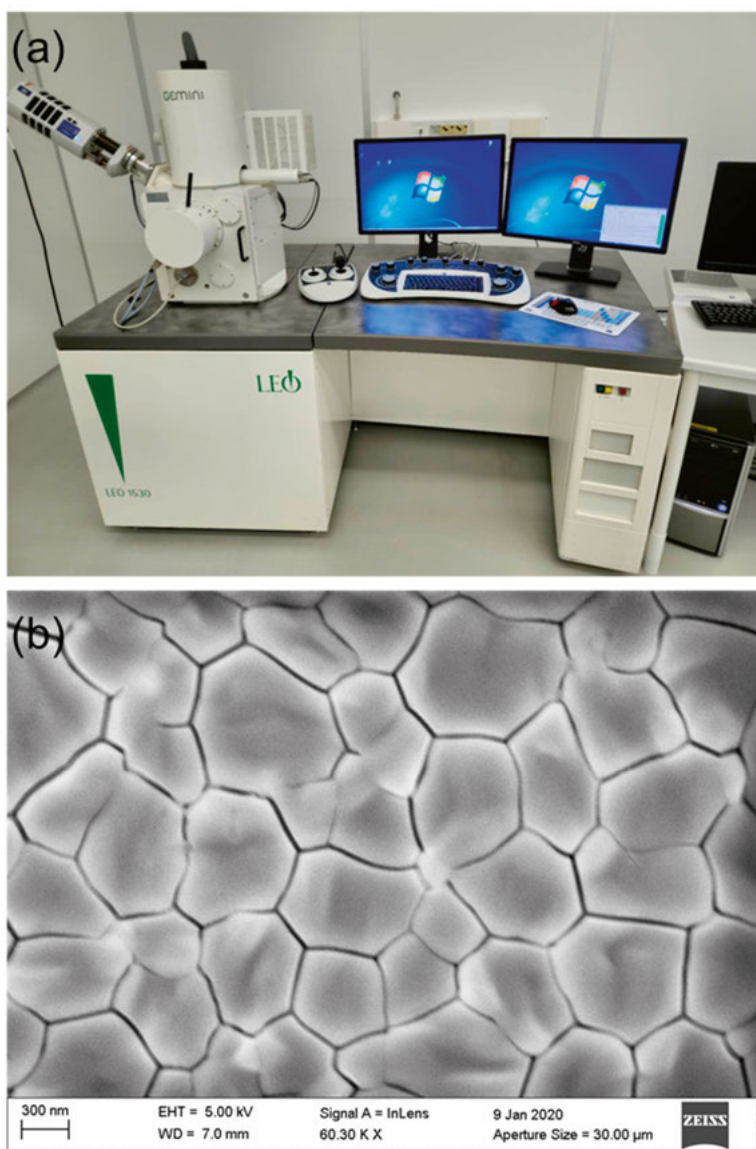


Figure 2-2 (a) The Zeiss LEO microscopes we used in our thesis and (b) the SEM image of perovskite film we took from this equipment.

Characterization of PSCs

The photovoltaic characteristics of the PSCs were assessed through the $J-V$ measurements and the incident photon-to-electron conversion efficiency (IPCE). The $J-V$ curves were measured under an irradiation intensity of 100 mW cm^{-2} by Wave Labs SINUS-70 solar simulator with UV and IR range

extenders giving AM1.5G spectral irradiance. The measurement of IPCE was measured by a homemade setup consisting of a Xenon lamp (Spectral Products ASB-XE-175), a monochromator (Spectral products CM110), and a Lab-Jack U6 data acquisition board.

Current Density-Voltage Measurement of Solar Cells

The photovoltage performance of solar cells is typically characterized by J - V curves (**Figure 2-3**). The J - V curve is obtained through a procedure wherein a solar device is subjected to simulated sunlight, a varying bias voltage is continuously applied, and its resulting current density is measured. This curve provides crucial parameters that are pertinent to the power conversion efficiency (PCE): open circuit voltage (V_{oc}), short circuit current (J_{sc}), fill factor (FF), and maximum power point (P_{max}). These parameters have the following relationship with each other:

$$FF = \frac{P_{max}}{J_{sc} \times V_{oc}}$$

$$PCE = \frac{P_{max}}{P_{in}} = FF \times J_{sc} \times \frac{V_{oc}}{P_{in}} \times 100\%$$

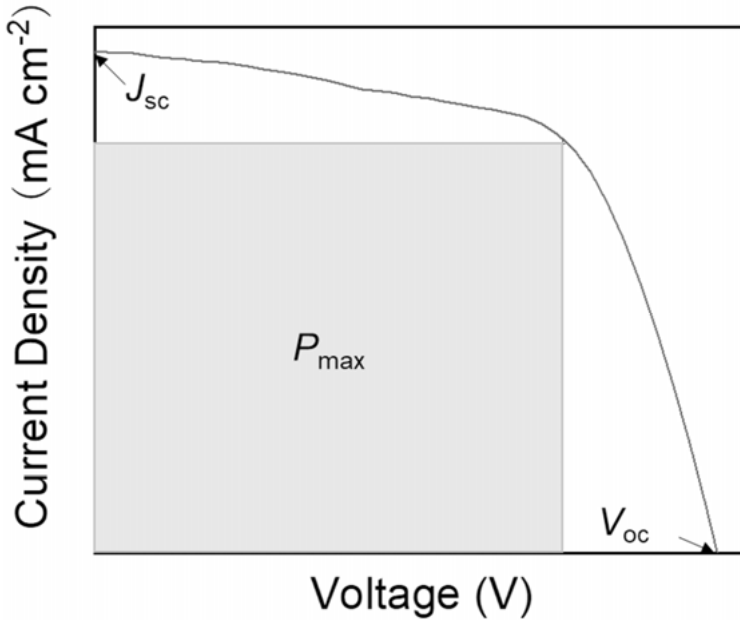


Figure 2-3 J - V curve of a solar cell.

As seen in **Figure 2-3**, the J_{sc} and V_{oc} can be obtained from a solar cell's output characteristics. J_{sc} can be derived at zero bias-voltage, while V_{oc} can be

determined when the current density reaches zero. The bandgap of the material has a close relationship with J_{sc} . The smaller the band gap, the greater the extent to which the material's absorption spectrum covers the solar spectrum, resulting in more photons being converted into current. J_{sc} is also related to the device's thickness and the transport properties of the carriers. The energy gap between n-type and p-type materials greatly determines V_{oc} . The V_{oc} is also influenced by the performance of the interface, the electrode contact, and charge recombination within the device. The FF reflects the ideal performance of the device diode and is impacted by the current. P_{max} represents the ideal working state of the solar cells, and the ratio of P_{max} to the incident light power is the PCE of the device.

Incident Photon-to-Current Efficiency

IPCE is a crucial value that assesses how well a solar cell or photovoltaic device can convert incoming light into electrical current. This value is displayed as a percentage and is calculated by dividing the photocurrent produced by the device by the flux of incident light photons. The IPCE is a significant factor that is used to gauge the performance of a solar cell and to compare it with other similar devices.

In a typical experiment, a solar cell device was placed in a sample holder and covered by a mask to regulate the amount of light absorbed by the sample. The light source was a Xenon lamp connected to a monochromator, allowing precise wavelength control. The monochromator was linked to a filter wheel and computer terminal. The light emitted from the monochromator and filter wheel was then divided using a beam splitter, with a portion of the light illuminating a reference silicon diode. The remaining light was directed toward the sample behind the mask. The sample and reference diode were connected through wires and contacts to an acquisition device, which transmitted the signal back to the computer. Before each experiment, a second reference silicon diode was used for calibration purposes, taking the place of the sample.

Conductivity

Equation (1) can be used to determine the DC (direct current) conductivity (σ_0)⁷³ by analyzing the slope of the I-V (current -voltage) plots:

$$I = \sigma_0 A l^{-1} V \quad (1)$$

where A is the sample area, and l is the thickness of the films.⁷⁴

Space-Charge-Limited-Current

Space-Charge-Limited-Current (SCLC) is a phenomenon that occurs in solid-state electronic devices, such as diodes and transistors, when the space charge

within the device limits the flow of charge carriers (electrons or holes). The space charge accumulates positive and negative charges within a material arising from imbalanced carrier injection or recombination. In an SCLC device, the flow of charge carriers is restricted by the space charge, leading to a current flow that is proportional to the square of the applied voltage. This results in a nonlinear current-voltage (I-V) characteristic for the device. The SCLC phenomenon is generally observed in devices with low carrier concentration and mobility, such as semiconductor thin films. SCLC can affect the performance of electronic devices in several ways, including limiting the maximum achievable current, causing current instabilities, and reducing the device's response time. Understanding and modeling the SCLC behavior of a device is important for optimizing its performance and developing new, high-performance devices.

This thesis measured the hole-related trap-state density n_{trap} of different samples using the SCLC method with an FTO/PEDOT: PSS/Perovskite/HTMs/Au structure. V_{TFL} is the trap-filled limit voltage determined by the trap states.⁷⁵⁻⁷⁷ Thus, n_{trap} could be calculated by equation (2).⁷⁷

$$n_{trap} = \frac{2\epsilon_0\epsilon V_{TFL}}{eL^2} \quad (2)$$

where L is the thickness of the perovskite film, ϵ_0 is the vacuum permittivity, e is the elementary charge, and ϵ is the dielectric constants of FAPbBr₃.^{66, 78}

Additionally, the SCLC method can be used to measure hole mobility. The preparation of HTLs was the same as the previous report,⁷⁹ employing a diode configuration of ITO/PEDOT: PSS/HTMs/Au for holes by measuring the dark current density in a suitable voltage range. The results were fitted to a space charge limited form, where equation (3) describes the SCLC:

$$J = \frac{9\epsilon_0\epsilon_r\mu_h V^2}{8L^4} \quad (3)$$

where J is the current density, ϵ_r is the relative dielectric constant of the transport medium, ϵ_0 is the permittivity of free space, V is the internal voltage in the device, L is the film thickness of the active layer, and μ_h is the hole mobility.

Results and discussion

This section presents the results and discussion of papers I-V, primarily focusing on the thorough investigation and characterization of FAPbBr₃ devices and their use in Photoelectrochemical (PEC) water-splitting applications.

Perovskite crystal growth control by the additives and solvent engineering

In this chapter, we report methods of optimizing the perovskite crystal by additions and utilizing a suitable solvent. There are limited studies on FAPbBr₃ previously.^{62, 67} Despite the very promising properties of stability and high voltage, the photovoltaic performance of this material still requires improvement.⁸⁰⁻⁸²

Applying the MABr additive can significantly enhance the quality of the perovskite films³² and address any Br deficiencies present in the film. Other additives, such as MACl, have also been found to promote the growth of perovskite crystals in FAPbI₃-based perovskite films.¹¹ Additionally, a suitable solvent is critical for converting PbX₂ into the perovskite form.⁸³⁻⁸⁵ In **papers I and II** of this thesis, two methods for preparing FAPbBr₃-based PSCs by adding additives into precursor solution and optimizing the solvent of FABr solution are developed. The findings indicate the possibility of attaining high-quality perovskite films with large crystal sizes free of pinholes.

In Paper I

A two-step spin coating technique is employed to prepare FAPbBr₃ films of superior quality in the glove box. As depicted in **Figure 3-1a**, MABr, DMSO, and MACl are leveraged to manufacture these films. MABr and MACl are added to the FABr solution to optimize film quality. Including MACl improves the crystallization of the FABr-PbBr₂-DMSO intermediate phase, promotes the generation of FAPbCl_{3-x}Br_x perovskite seeds, and triggers the transition of perovskite phase and growth of the crystal.⁸⁶ As revealed by the SEM images in **Figure 3-1b**, the perovskite on the samples is uniformly distributed without any observable pinholes. Furthermore, adding additives increased the

grain size. The findings demonstrate that the presence of additives substantially affects the grain size of the FAPbBr_3 material.

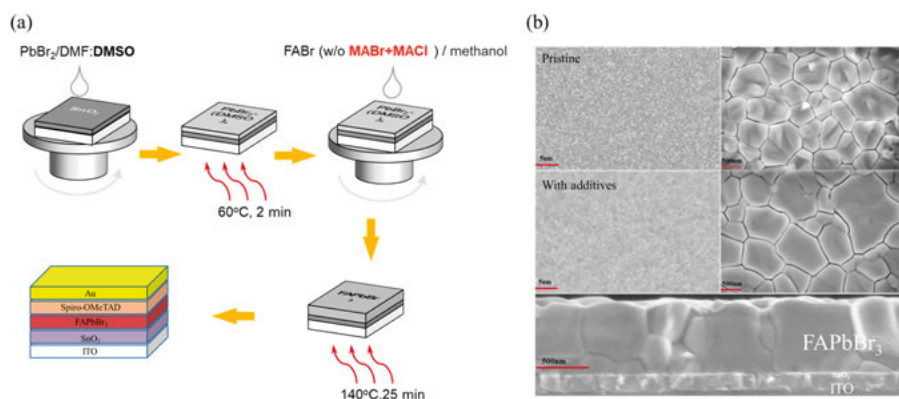


Figure 3-1 (a) The illumination of the fabrication process in the glove box. (b) SEM images of FAPbBr_3 films on rigid glass/ITO/SnO₂ substrate.

From **Figure 3-2a**, adding additives to the perovskite films resulted in XRD peaks with a stronger intensity than the unmodified perovskite film, suggesting an improvement in crystallinity.⁸⁷ The (100) peak of the perovskite film with additives has shifted slightly toward higher angles, possibly due to the larger ionic radius of FA^+ (2.79 Å) than that of MA^+ (2.70 Å).^{62, 63} It, therefore, suggests that MA exists in the perovskite fabricated with additives.⁸⁸ Considering the effect of Cl in the growth of perovskite crystals and the adjustment of the layer morphology, it seems that the introduction of MACl plays a crucial role in perovskite crystallization.¹¹ The SSPL intensity in **Figure 3-2b** has increased with additives. Further, it has been shown that the device with additives results in higher PCE, which could be associated with increased radiative recombination, resulting in high V_{oc} and J_{sc} . It is worth mentioning that the Pb 4f XPS spectra for the unmodified perovskite film reveal two smaller peaks located around 135 and 140 eV, indicating the presence of metallic Pb⁰.⁸⁹ The Pb⁰ defects serve as nonradiative recombination centers,⁸⁷ which are negatively impacting the transport and collection of photogenerated charge-carriers.⁹⁰ In comparison, these two peaks are not observed in the sample with additives, indicating a reduction in metallic lead content, which is advantageous for the photovoltaic performance of solar cell devices.

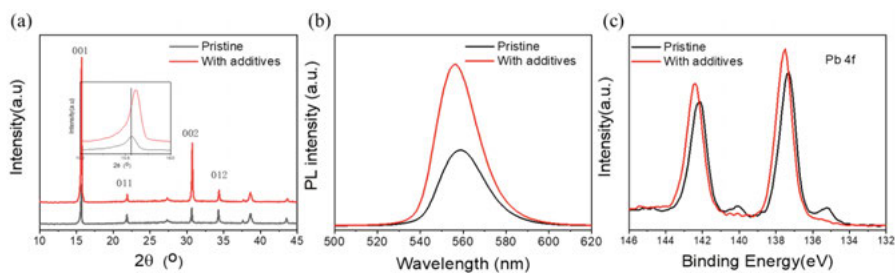


Figure 3-2 (a) XRD patterns, (b) SSPL, and (d) XPS spectra of FAPbBr₃ films on rigid glass/ITO/SnO₂ substrate.

The photovoltage performance results are shown in **Figures 3-3** and **Table 1**. The pristine device showed a PCE of 6.6% for the rigid devices. In comparison, the device with additives achieved a higher PCE of 7.9% with minimal hysteresis. Similarly, the PCE of the flexible devices shows a similar trend. The attached paper presents photovoltaic statistics parameters demonstrating the device's good reproducibility.

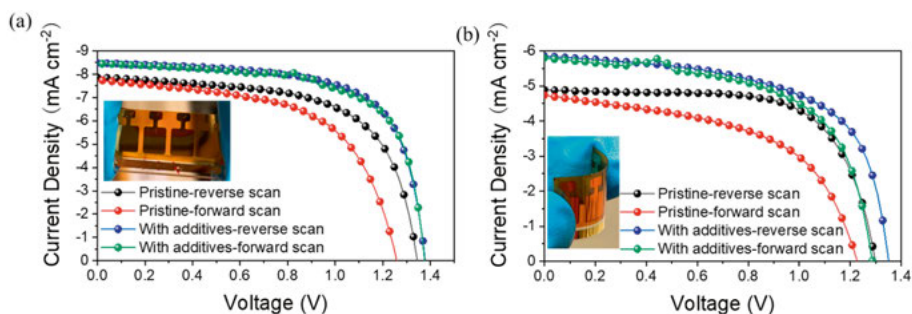


Figure 3-3 The J - V characteristics of FAPbBr₃-PSCs on (a) rigid and (b) flexible substrates under AM 1.5G one sun illumination (100 mW/cm²).

Table 1. Device parameters for champion PSCs without and with additives.

| Device | | PCE (%) | FF (%) | J_{sc} (mA cm ⁻²) | V_{oc} (V) |
|--|--------------|---------|--------|---------------------------------|--------------|
| Pristine on the rigid substrate | Reverse scan | 6.6 | 62.8 | -7.86 | 1.34 |
| | Forward scan | 5.6 | 57.8 | -7.76 | 1.25 |
| With additives on the rigid substrate | Reverse scan | 7.9 | 67.7 | -8.48 | 1.37 |
| | Forward scan | 7.7 | 66.6 | -8.46 | 1.37 |
| Pristine on the flexible substrate | Reverse scan | 4.3 | 67.9 | -4.89 | 1.29 |
| | Forward scan | 3.1 | 52.9 | -4.74 | 1.22 |
| With additives on the flexible substrate | Reverse scan | 5.0 | 60.5 | -5.93 | 1.37 |
| | Forward scan | 4.5 | 59.4 | -5.87 | 1.30 |

In conclusion, the additives of MABr and MACl were applied in the FABr solution, leading to increased perovskite crystal size and enhanced crystallinity perovskite film from SEM and XRD results. Both rigid flexible PSCs that utilized these additives exhibited better photovoltaic performance than the control samples. Our results provided a straightforward and effective method for enhancing the performance of the FAPbBr₃-PSCs made in the glove box.

In Paper II

For the first work, the FAPbBr₃ was synthesized using the conventional method in a glove box. However, a more scalable and low-cost fabrication process is necessary for practical and commercial applications. In the second study, **all the steps in producing the FAPbBr₃-PSCs were performed in ambient environmental conditions.** This work utilized a two-step process to

fabricate the FAPbBr_3 perovskite film. The PbBr_2 layer was first deposited on the SnO_2 substrate, followed by the deposition of the FABr solution onto the PbBr_2 layer. The fabrication process was optimized by adjusting the spin-coating speed and the concentration of the solution. These adjustments accounted for the different environments in which the fabrication took place. The PbBr_2 layer was deposited on the SnO_2 layer, then the FABr dissolved in different solvents (IPA, MeOH, and Mixed IPA/MeOH) were deposited on the PbBr_2 film. The solvents have different viscosity and polarity, leading to different perovskite crystallization processes. However, the high viscosity of the IPA hindered the effective diffusion of FABr into the PbBr_2 , causing a rough surface and poor perovskite conversion.⁸³ The low viscosity and high solubility for MeOH solvent lead to effective diffusion of FABr into the PbBr_2 . But the strong polarity of MeOH will dissolve and destroy part of the perovskite during spin coating.⁸³ A mixture of IPA and MeOH with finely controlling the ratio of IPA and MeOH can balance viscosity, polarity, and solubility, leading to the effective diffusion of FABr into the PbBr_2 and minimizing the perovskite loss during spin coating processes. **Figures 3-4 b and c** demonstrate that FABr is highly soluble in MeOH, and the IPA/MeOH mixed solvent, which is attributed to the high polarity and solubility of MeOH. Pure MeOH dissolves part of the perovskite layer. Due to the relatively low polarity of IPA, the perovskite layer does not easily decompose in the mixed IPA/MeOH solvents.

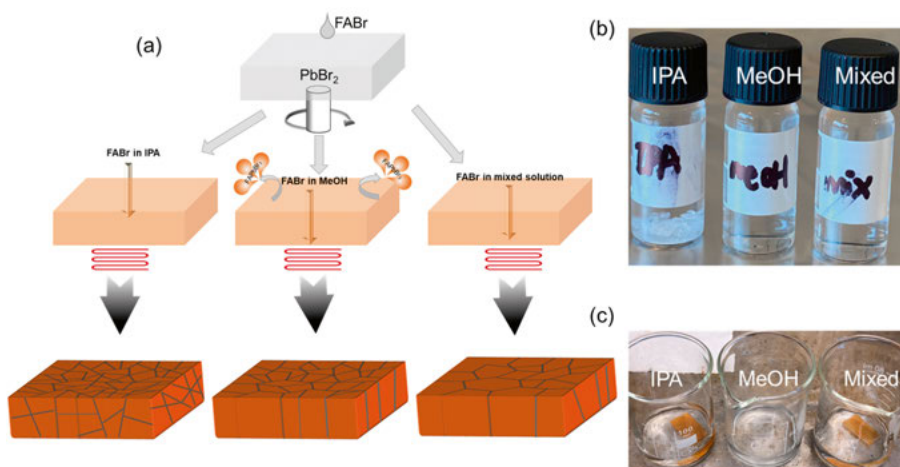


Figure 3-4 (a) A schematic illustration is shown to depict the growth process of the FABr perovskite in different solvents in ambient environmental conditions. (b) FABr dissolved in different solvents. (c) FAPbBr_3 was placed in different solvents.

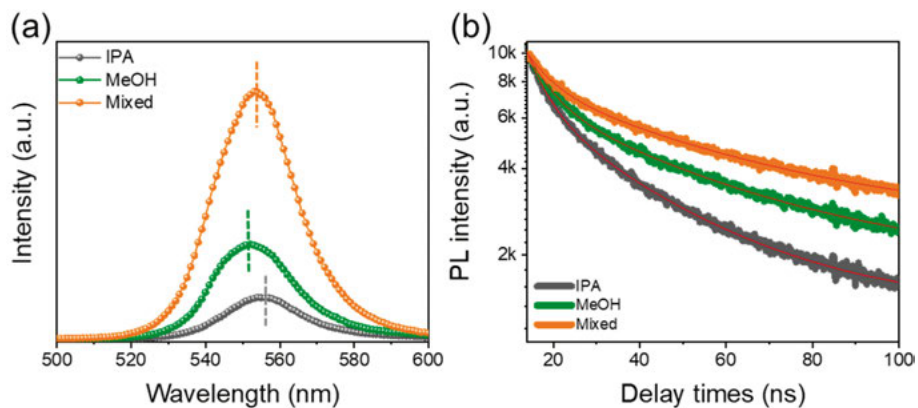


Figure 3-6 (a) SSPL and (b) TRPL for different solvent-prepared perovskite films.

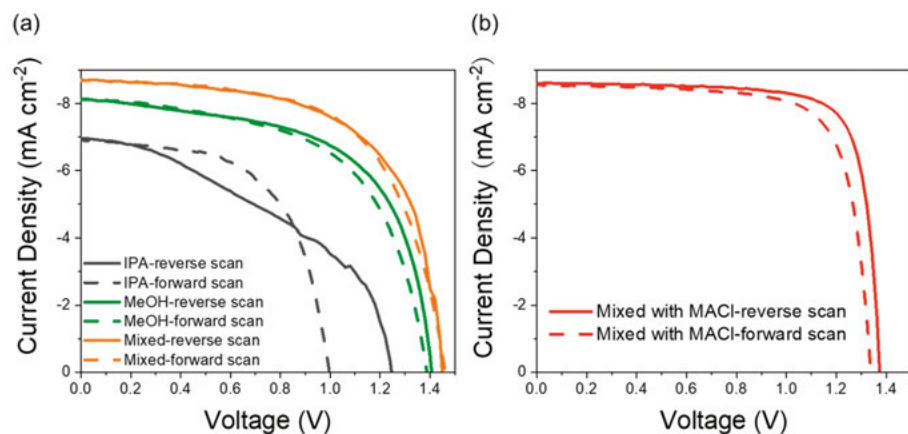


Figure 3-7 J - V curves (a) for the samples prepared with different solvents and (b) curves of the devices made by mixed solvent with MACl additive.

Finally, the photovoltage performance of the different devices is displayed in **Figure 3-7a** and Table 2. The mixed solvent sample got the highest PCE of 7.87%. However, efficiency still requires improvement. Our first work reported that using MACl as an additive could result in high-quality FAPbBr_3 PSCs with high FF and PCE.¹ So, the same strategy was applied in this work. As shown in **Figure 3-7b** and Table 2, adding MACl in the mixed solvent solution improved the device efficiency to 9.26% with a high FF of 78%, and it also shows the good repeatability in the attached paper from the photovoltaic statistics parameters.

Table 2. Photovoltaic parameters of the devices prepared with different solvents.

| device | PCE (%) | FF (%) | J_{sc} (mA.cm ⁻²) | V_{oc} (V) |
|-------------------------------------|---------|--------|---------------------------------|--------------|
| IPA- Reverse | 3.69 | 42.66 | -6.96 | 1.24 |
| IPA- Forward | 4.07 | 59.16 | -6.91 | 1.00 |
| Methanol- Reverse | 6.88 | 60.17 | -8.13 | 1.40 |
| Methanol- Forward | 6.56 | 58.10 | -8.14 | 1.39 |
| Mixed- Reverse | 7.87 | 62.55 | -8.71 | 1.44 |
| Mixed- Forward | 7.84 | 61.70 | -8.69 | 1.46 |
| Mixed solvent With MACl- Reverse | 9.26 | 78.04 | -8.60 | 1.38 |
| Mixed solvent With MACl- Forward | 8.52 | 74.26 | -8.56 | 1.34 |

In conclusion, this work demonstrates the effectiveness of solvent engineering by mixing IPA and MeOH, leading to improved quality perovskite films and higher PCEs compared to using the individual solvents. Adding a small amount of MACl into the mixed solvent solution further enhanced the performance, resulting in a PCE of 9.26% under ambient preparation conditions.

Passivation of the defects on the perovskite by 2D perovskite

As well known, defects, such as grain boundary or surface defects, are major factors affecting device performance.³³⁻³⁵ The interfacial defects also cause significant hysteresis in the $J-V$ characteristics due to ion migration and lifetime degradation due to the moisture accumulation at these defects.^{34, 36-38} In iodide-based PSCs, many studies have reported using low-dimensional perovskites as a passivating layer on 3D perovskite films to address these issues.⁹⁴⁻⁹⁶ The organic spacer cations in low-dimensional perovskites are often hydrophobic and result in greater stability due to these hydrophobic cations.^{39, 97} To improve photovoltage performance and stability in FAPbBr₃-PSCs, in **paper III**, we employed 2D perovskite as a passivating layer on the surface of 3D perovskite to address the interface defects.

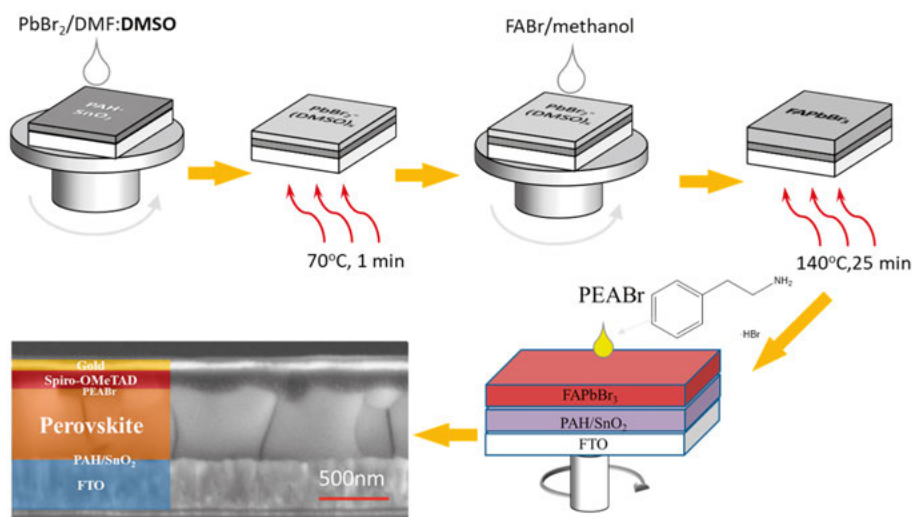


Figure 3-8 The schematic structure and diagram of the 2D perovskite layer preparation on the 3D lead bromide perovskite.

Figure 3-8 shows the two-step spin-coated method to fabricate the FAPbBr₃-perovskite films (3D perovskite films). Then the PEABr solution was deposited on the FAPbBr₃ film without thermal annealing. The XRD results confirmed the crystal structure of the perovskite films, as demonstrated in **Figures 3-9a** and **b**. The 2D (PEA)₂PbBr₄ structure peak was observed in samples treated with PEABr.^{98, 99} The treatment of 1.25 mg mL⁻¹ PEABr increased the intensity of the main diffraction peaks of FAPbBr₃, which are located at 14.8° and 29.7°. This enhancement in intensity indicates an improvement in the

crystallinity of the perovskite films. Moreover, the SSPL and UV-vis absorption spectra revealed evidence of $(\text{PEA})_2\text{PbBr}_4$ structure, as shown in **Figures 3-9c and 3-9d**, respectively, with a small peak observed around 410 nm.⁹⁸ The PEABr-modified film also demonstrated a higher PL intensity than the pristine film, implying a reduced number of interface defects and better quality of the perovskite film. Also, the PEABr-modified perovskite film showed slightly enhanced absorption, which may be the result of the improved crystallinity and lead to the enhanced J_{sc} .^{100, 101}

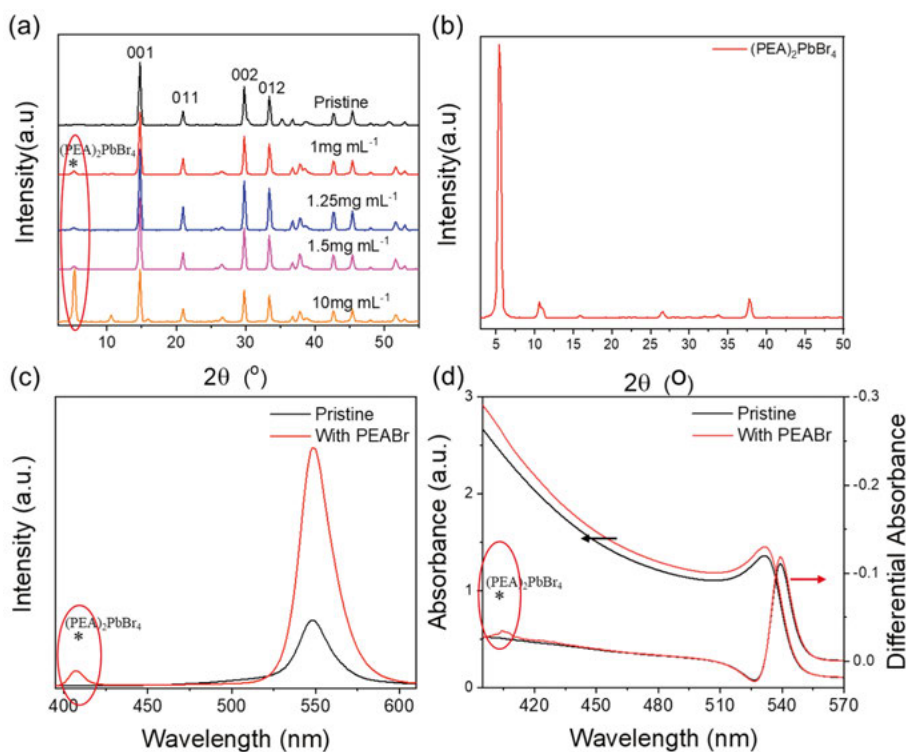


Figure 3-9 (a) XRD for the perovskite films with and without surface modification with 2D perovskite prepared using different concentrations of the PEABr, (b) XRD for the $(\text{PEA})_2\text{PbBr}_4$ perovskite film, (c) SSPL and (d) UV-vis absorption spectra of the perovskite films with and without PEABr treatment.

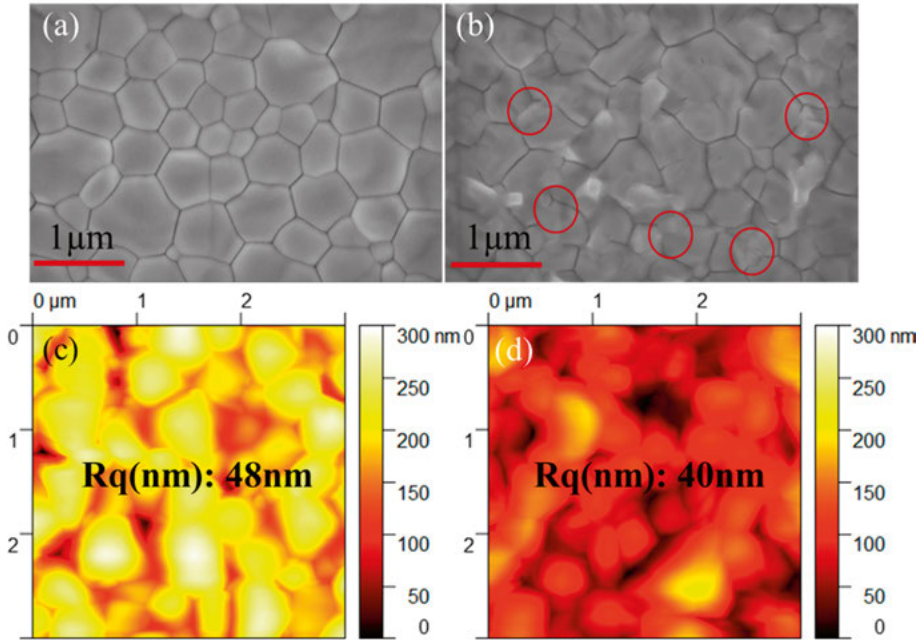


Figure 3-10 SEM images of the perovskite films (a) Pristine, (b) with PEABr treatment. Red circles are examples of regions where differences are observed in surface morphology. Atomic Force Microscopy (AFM) images of the perovskite films (c) Pristine, (d) with PEABr treatment.

Figure 3-10 shows the surface morphology of perovskite films taken by SEM and AFM. The presence of a 2D perovskite caused differences in the surface morphology for the sample with PEABr treatment. The PEABr-treated sample also shows a smoother surface, which can promote the deposition of HTM layers, reduce series resistance to accelerate charge transport¹⁰², and increase shunt resistance due to better coverage of the HTM and lower recombination at the interface.

Figure 3-11 shows that the SCLC measurement was applied to study the hole-related trap density (n_{trap}) of the perovskite films.⁷⁶ The PEABr-treated sample presented a lower n_{trap} than the pristine sample, indicating that 2D perovskite can passivate the interface defects.¹⁰³

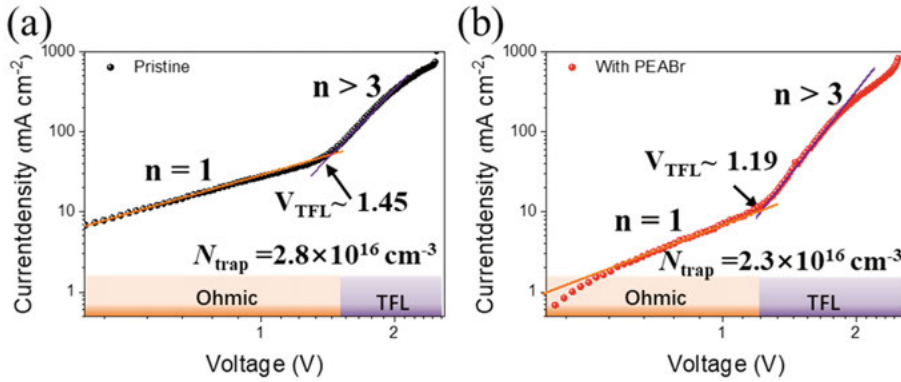


Figure 3-11 The J - V measurement of hole-only devices in the dark for determining the n_{trap} , (a) Pristine, (b) With PEABr. The structure of the hole-only devices is (FTO/PEDOT: PSS/FAPbBr₃/ (with or without PEABr) /Spiro-OMeTAD/Au).

The J - V curve and stability of the devices are shown in **Figure 3-12** and **Table 3**. The pristine device exhibited a lower PCE of 7.6% than the PEABr treatment device (9.4%), and all samples show good repeatability from the photovoltaic statistics parameters in the attached paper. The improvement in the FF of the devices was significant with the PEABr treatment and was the main contributor to the improvement of the PCE. A key factor in improving the FF is the reduction of defect-induced recombination. As shown in **Figure 3-12b**, the enhanced stability of the PEABr-treated device was attributed to the shielding effect of the hydrophobic organic spacer cation present in PEABr compared to the untreated device. This was verified by the water contact angle measurement, which exhibited that the PEABr-treated perovskite film had higher hydrophobicity and better moisture stability compared to the untreated perovskite film.

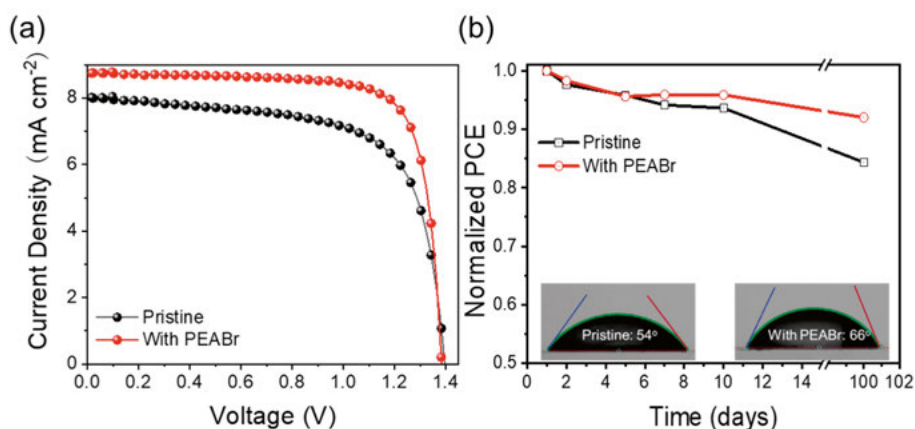


Figure 3-12 (a) J - V and (b) Long-term stability measurement of PSCs with and without PEABr modification. The inset image shows the water contact angle measurements for pristine and PEABr-modified perovskite films.

Table 3. Photovoltaic parameters of the PSCs with and without PEABr modification.

| Devices | PCE (%) | FF (%) | J_{sc} (mA.cm ⁻²) | V_{oc} (V) | R_{shunt} (Ohm.cm ²) | R_{series} (Ohm.cm ²) |
|------------|---------|--------|---------------------------------|--------------|------------------------------------|-------------------------------------|
| Pristine | 7.6 | 67.6 | 8.0 | -1.4 | 2605.0 | 9.2 |
| With PEABr | 9.4 | 77.6 | 8.8 | -1.4 | 6306.4 | 5.0 |

For the conclusion of the third work, we successfully applied a 2D PEA_2PbBr_4 perovskite onto 3D $FAPbBr_3$ to passivate the interface defects by depositing the PEABr solution on the 3D perovskite. The reduced trap density, reduced series resistance, and increased shunt resistance enhanced the photovoltaic performance of the PEABr-treated device. The hydrophobic organic spacer cations in 2D perovskite also improved the stability of the PEABr-treated device.

Acceleration of hole extraction by using dopant-free hole transport materials

Paper II showed that the doped Spiro-OMeTAD-based FAPbBr₃-PSCs were unstable when fabricated in the ambient environment. The hydrophilic nature of the dopants may cause many pinholes in the sample surface, as shown in **Figure 3-13**. In **paper IV**, dopant-free hole transport materials were applied to continue investigating the FAPbBr₃ solar cell made in ambient conditions.

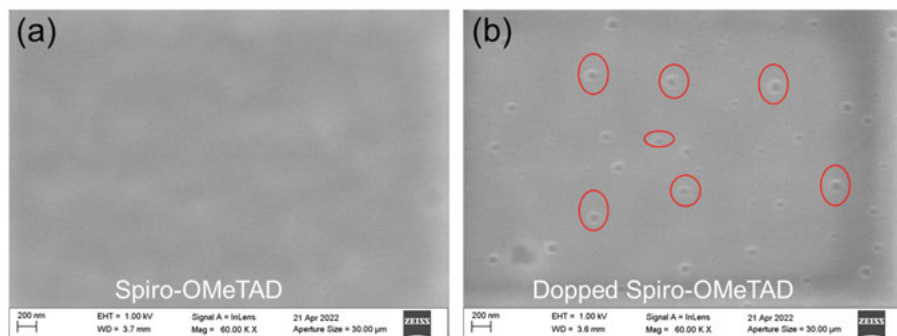


Figure 3-13 SEM images of the perovskite films with (a) undoped Spiro-OMeTAD and (b) lithium salt-doped Spiro-OMeTAD.

Among the HTMs used in PSCs, Spiro-OMeTAD is one of the most frequently utilized. However, despite its popularity, the dopant-free version of Spiro-OMeTAD suffers from intrinsic low hole mobility and poor conductivity. This is attributed to its triangular pyramid configuration and large intermolecular distance.¹⁰⁴ At the same time, the dopants (such as Li-TFSI) would cause stability problems and degradation of the devices due to the ion immigration and hydrophilic nature⁴²⁻⁴⁶. Therefore, it encourages the utilization of different dopant-free hole-transport materials into PSCs, such as PTB7, TQ1, and P3HT.^{47, 48, 105-107}

Figures 3-14a and **b** show the highest occupied molecular orbital (HOMO) levels of the four HTMs. The lower HOMO energy levels of P3HT film better match the valence band of the FAPbBr₃. Also, **Figures 3-14c** and **d** demonstrate that the P3HT film has higher hole mobility and conductivity than Spiro-OMeTAD due to the different structure. Head-to-tail coupled P3HT films with high regioregularity (RR) allows obtaining planar conformations of polymers characterized by extended π -conjugation and organization in large crystalline domains, which contribute to enhancing the hole mobility.^{105, 108} Therefore, P3HT is expected to extract photogenerated carriers from the perovskite

absorbers more efficiently.¹⁰⁹ Also, sulfur atoms in P3HT can bind with Pb^{2+} , which might remove parts of the perovskite grain crystal defects.

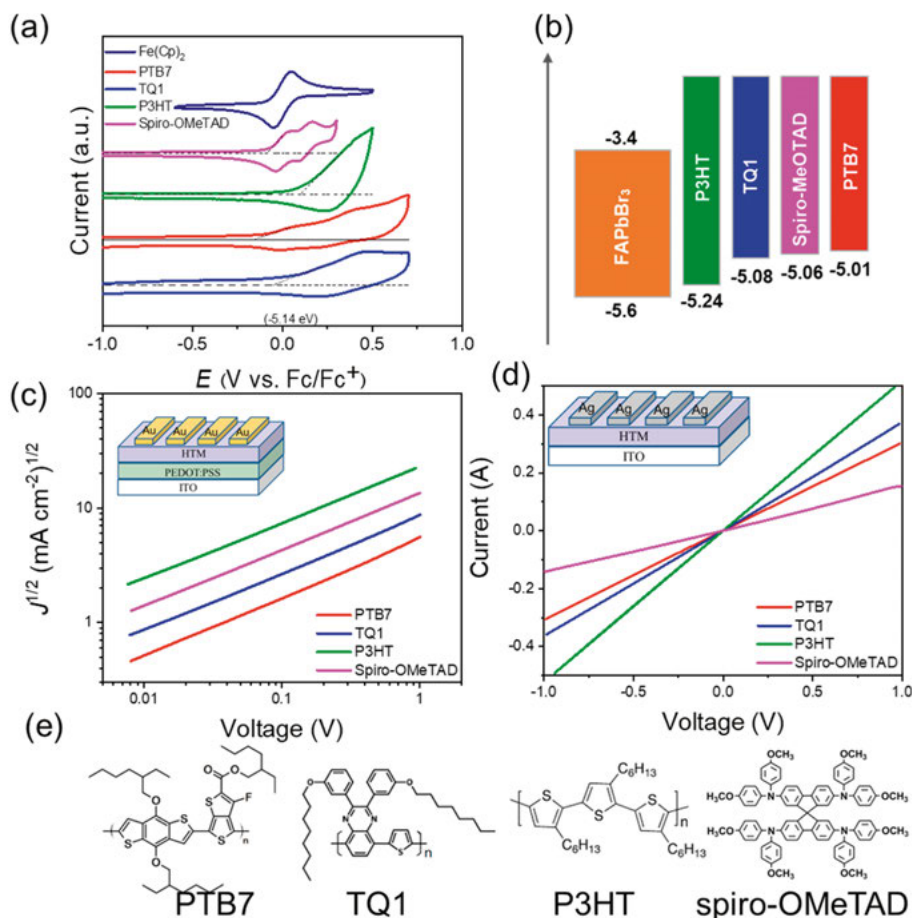


Figure 3-14 (a) Cyclic voltammogram (CV), (b) energy level diagram, (c) J - V curves of the hole-only devices for HTMs in the SCLC region, (d) conductivity and (e) chemical structures of different HTMs (PTB7, TQ1, P3HT, and spiro-OMeTAD).

Figures 3-15a and **b** show the light absorption and IPCE for the solar cells with dopant-free HTLs. From UV-Vis measurements, the HTLs have different absorption. Polymer HTLs samples have a broader absorption peak from 350 to 750 nm compared to spiro-OMeTAD, which shows light absorption at 350-550 nm. **Figures 3-15b, c,** and **Table 4** show the IPCE and photovoltage performance of the different samples. The P3HT-PSCs show the highest PCE due to the enhanced V_{oc} and FF. Also, the P3HT-PSCs show the highest

photogenerated current efficiency. The enhanced IPCE may be caused by improved charge dissociation and reduced recombination.¹¹⁰ In **Figures 3-16c** and **d**, SSPL and TRPL were used to examine the interfacial charge transfer kinetics of different dopant-free HTLs deposited on the perovskites. P3HT shows the lowest PL peak intensity and shortest lifetime, indicating a faster hole extraction capability.

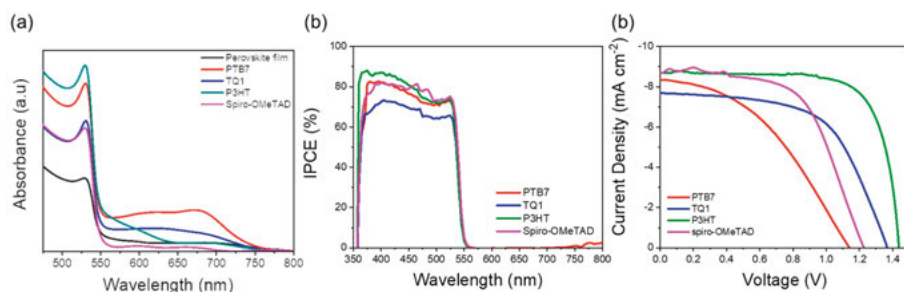


Figure 3-15 (a) UV-vis absorption, (b) IPCE, (c) J - V curve of perovskite, perovskite-PTB7, perovskite-TQ1, perovskite-P3HT, and perovskite-spiro-OMeTAD.

Table 4. Summary of the photovoltaic parameters for the different dopants-free HTLs-PSCs.

| HTLs | PCE (%) | J_{sc} (mA cm ⁻²) | FF | V_{oc} (V) |
|--------------|---------|---------------------------------|-------|--------------|
| PTB7 | 3.93 | -8.36 | 41.19 | 1.14 |
| TQ1 | 6.17 | -7.69 | 58.68 | 1.36 |
| P3HT | 9.38 | -8.74 | 73.26 | 1.47 |
| Spiro-OMeTAD | 6.30 | -8.75 | 58.67 | 1.23 |

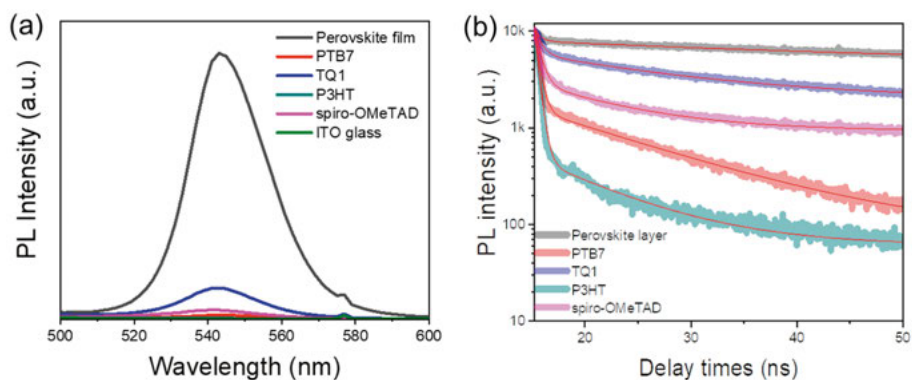
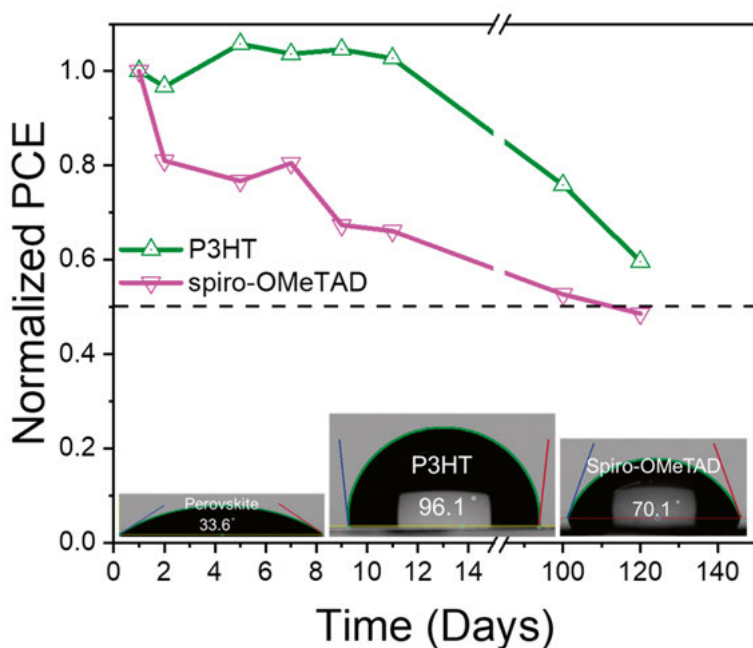


Figure 3-16 (a) SSPL and (b) TRPL of perovskite, perovskite-PTB7, perovskite-TQ1, perovskite-P3HT and perovskite-spiro-OMeTAD.



Figures 3-17 Long-term stability measurement of PSCs different HTLs. The inset image shows the water contact angle measurements for perovskite film and with different HTLs.

As mentioned above, this work aims to improve the stability of devices prepared in ambient conditions. The stability data of different dopant-free devices are shown in **Figure 3-17**. The devices were stored in dry box conditions without encapsulation. The PSCs with P3HT show better stability than PSCs with

spiro-OMeTAD. The water contact angles measurement compared the influence of the hydrophobic nature of dopant-free HTLs on the perovskite layer. The hydrophobic properties of the P3HT act as a moisture barrier to protect the device, resulting in a higher water contact angle than the sample with spiro-OMeTAD on perovskite.

In conclusion, in the **paper IV**, we studied several different structures of dopant-free HTMs in FAPbBr₃-PSCs. Our results show that devices with P3HT present superior photovoltage performance due to higher hole mobility of P3HT, lower interface trap density with P3HT, and faster hole transfer from the perovskite to P3HT. We achieved the highest performance in FAPbBr₃-PSCs based on dopant-free P3HT with an outstanding PCE of 9.38%. The dopant-free P3HT also leads to improved stability.

Integration of carbon electrode and FAPbBr₃ for photovoltaic and photoelectrochemical application

During the **paper IV**, we noticed that even though dopant-free-P3HT devices showed better stability than dopant free- spiro-OMeTAD-devices. The stability still needs to improve since the efficiency decreased by 40% after four months.

In most standard structures, configurations with organic HTLs and metal electrodes, the dopants in the HTL are necessary for high conductivities and mobility to reach high PCE, while the dopant also leads the device to unstable and degradation.⁴¹⁻⁴⁶ The expensive metal electrodes also increase the device cost. To simplify the fabrication process and address the limitations associated with using HTLs in PSCs, researchers have explored the possibility of removing HTLs from the standard device structure (n-i-p). Perovskite materials typically exhibit ambipolar properties with combined electron- and hole conductivity, which reduces the need for an additional HTL.⁴⁹ Carbon was selected as the hole extraction electrode for PSCs due to its affordability to resist ion migration and water, and good energy level alignment with most perovskites. In addition, carbon enables simpler and more accessible fabrication techniques, such as doctor-blade or screen-printing methods, as opposed to the high vacuum evaporation required for metal electrodes. Moreover, the carbon electrode will not damage the perovskite layer.¹¹¹ In **Paper V**, we fabricated HTL-free PSCs using carbon electrodes, successfully enhancing the devices' stability and producing impressive photovoltaic performance.

Due to the intermittency of solar energy, it is necessary to develop energy storage systems to store surplus energy for use during periods of low sunlight. In recent years, hydrogen production has gained significant attention as a promising option for long-term energy storage.¹¹² Using semiconductors submerged in an aqueous solution, photoelectrochemical (PEC) water splitting is a promising technology that directly splits water into oxygen and hydrogen using sunlight. It has been demonstrated that PEC water splitting is technologically and economically feasible for small and large-scale applications.¹¹³ Developing efficient PEC electrodes can save costs as the PV power generator, and electrolyzer can be integrated into a single system.¹¹³ However, developing efficient visible-light absorber materials that work as power generators, are cost-effective, and exhibit stability in water is still challenging.¹¹⁴ In our previous research (**paper I-IV**), we found that FAPbBr₃, possessing a high energy bandgap of 2.3 eV, produces a significantly higher photovoltage (exceeding 1.4 V) compared to I-rich PSCs, which typically generate photovoltages around 1.1 V. This is noteworthy because a photovoltage below 1.23 V is insufficient for water splitting. However, the high sensitivity of

perovskites to moisture is also a problem. To avoid contact between the perovskite and moisture, a FAPbBr₃-based perovskite photoelectrochemical cell (PEC) with a carbon electrode is utilized in this thesis, which shows impressive stability and efficiency. This work represents the first successful implementation of FAPbBr₃ in a PEC.

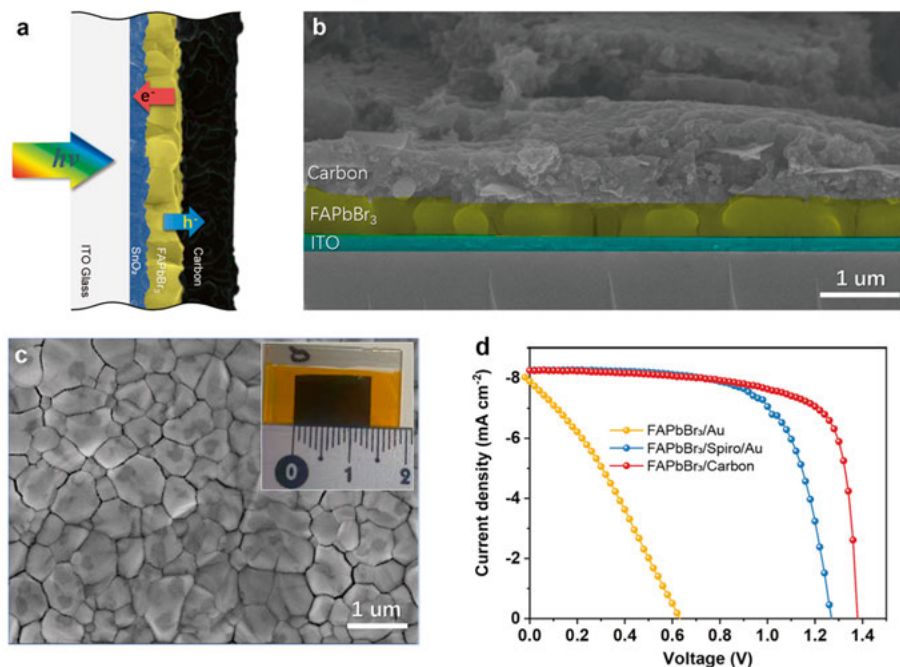


Figure 3-18 (a) Device structure of HTL-free FAPbBr₃ solar cell. SEM images of HTL-free FAPbBr₃/Carbon solar cell in (b) cross-section view and (c) top view. (d) Representative J - V curves of FAPbBr₃/Carbon solar cell and reference solar cells.

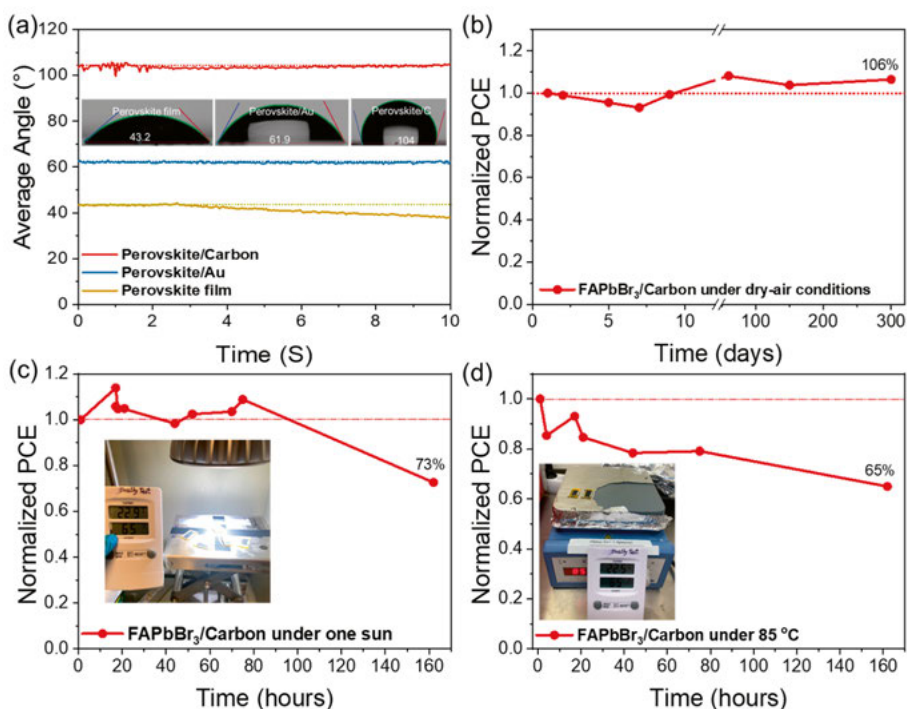


Figure 3-19 (a) Water contact angle analysis of FAPbBr₃/Carbon solar cell film and other reference films. Stability tests of FAPbBr₃/Carbon solar cell under (b) dry-air conditions, (c) one-sun conditions in ambient conditions, and (d) 85°C heating conditions in ambient conditions. All PSCs were totally made in ambient conditions.

As shown in **Figures 3-18a** and **b**, the device structure of the FAPbBr₃ solar cells is ITO-SnO₂-FAPbBr₃-Carbon. The perovskite layer thickness is around 400 nm for the sample. As shown in **Figure 3-18c**, the top view SEM image shows a good quality of perovskite films without pinholes. From the *J-V* curves in **Figure 3-18d** and **Table 5**, the champion device shows a PCE of 9.16% with a high V_{oc} of 1.38 V, J_{sc} of 8.69 mA cm⁻², and FF of 76.04%. It also shows the good repeatability in the attached paper from the photovoltaic statistics parameters.

Table 5. Device parameters devices.

| Device | PCE (%) | FF (%) | J_{sc} (mA.cm ⁻²) | V_{oc} (V) |
|-------------------------------|---------|--------|---------------------------------|--------------|
| FAPbBr ₃ /Au | 1.53 | 30.79 | -7.87 | 0.63 |
| FAPbBr ₃ /Spiro/Au | 7.13 | 67.97 | -8.26 | 1.27 |
| FAPbBr ₃ /Carbon | 9.16 | 76.04 | -8.69 | 1.38 |

Figure 3-19a shows the water contact angle of the FAPbBr₃/Carbon, FAPbBr₃/Au, and pristine FAPbBr₃ film; FAPbBr₃/Carbon exhibits a water contact angle (WCA) of 104°, which is larger than the gold sample (61.9°) and FAPbBr₃ film (43.2°). It is worth mentioning that the FAPbBr₃ film decomposed immediately after contact with water, leading to a decreased WCA with time. With the protection of the hydrophobic carbon layer, the FAPbBr₃/Carbon device showed 106% of its original efficiency under dry-air conditions after 360 days (**Figure 3-19b**). **Figures 3-20** and **Table 6** show the performance of fresh and aged samples: V_{oc} and FF parameters remain unchanged after 150 days; J_{sc} is even improved, which leads to the enhancement of PCE after 360 days of treatment. The photo-stability of FAPbBr₃/Carbon was evaluated under continuous one-sun illumination conditions: no performance decay was observed after 72 hours of illumination; the device kept 73% of its original efficiency even after 160 hours of illumination (**Figure 3-19c**). The corresponding ambient thermal stability was investigated under 85°C heating conditions. As shown in **Figure 3-19d**, the device PCE degraded to 80% after 72 hours of operation, which further decreased to 65% efficiency after 160 hours of heating. The high voltage, excellent stability, and hydrophobic nature of HTM-free FAPbBr₃/Carbon devices are beneficial to the building of FAPbBr₃-based photoelectrochemical water oxidation devices.

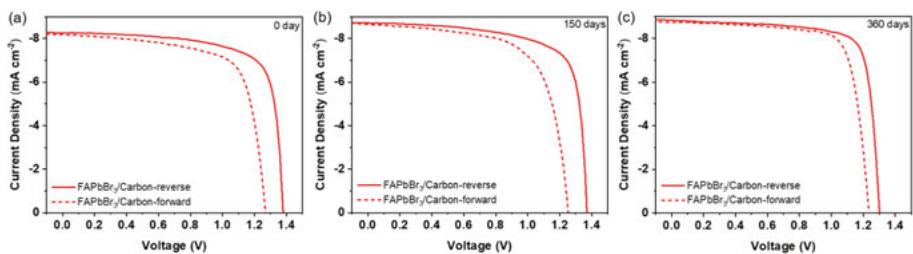


Figure 3-20 J - V curves of FAPbBr₃/Carbon solar cell. (a) pristine; aged under dry-air conditions for (b) 150 days and (c) 360 days.

Table 6. Device parameters for pristine and aged (dry-air conditions) FAPbBr₃/Carbon solar cells.

| Device | PCE (%) | FF (%) | J_{sc} (mA.cm ⁻²) | V_{oc} (V) |
|---|---------|--------|------------------------------------|--------------|
| Pristine FAPbBr ₃ /Carbon Reverse | 8.47 | 74.44 | -8.26 | 1.38 |
| Pristine FAPbBr ₃ /Carbon Forward | 7.29 | 70.23 | -8.18 | 1.27 |
| Aged (150 days) FAPbBr ₃ /Carbon Reverse | 8.79 | 73.60 | -8.74 | 1.37 |
| Aged (150 days) FAPbBr ₃ /Carbon Forward | 7.20 | 66.33 | -8.65 | 1.26 |
| Aged (360 days) FAPbBr ₃ /Carbon Reverse | 9.02 | 78.42 | -8.83 | 1.30 |
| Aged (360 days) FAPbBr ₃ /Carbon Forward | 8.26 | 76.38 | -8.75 | 1.24 |

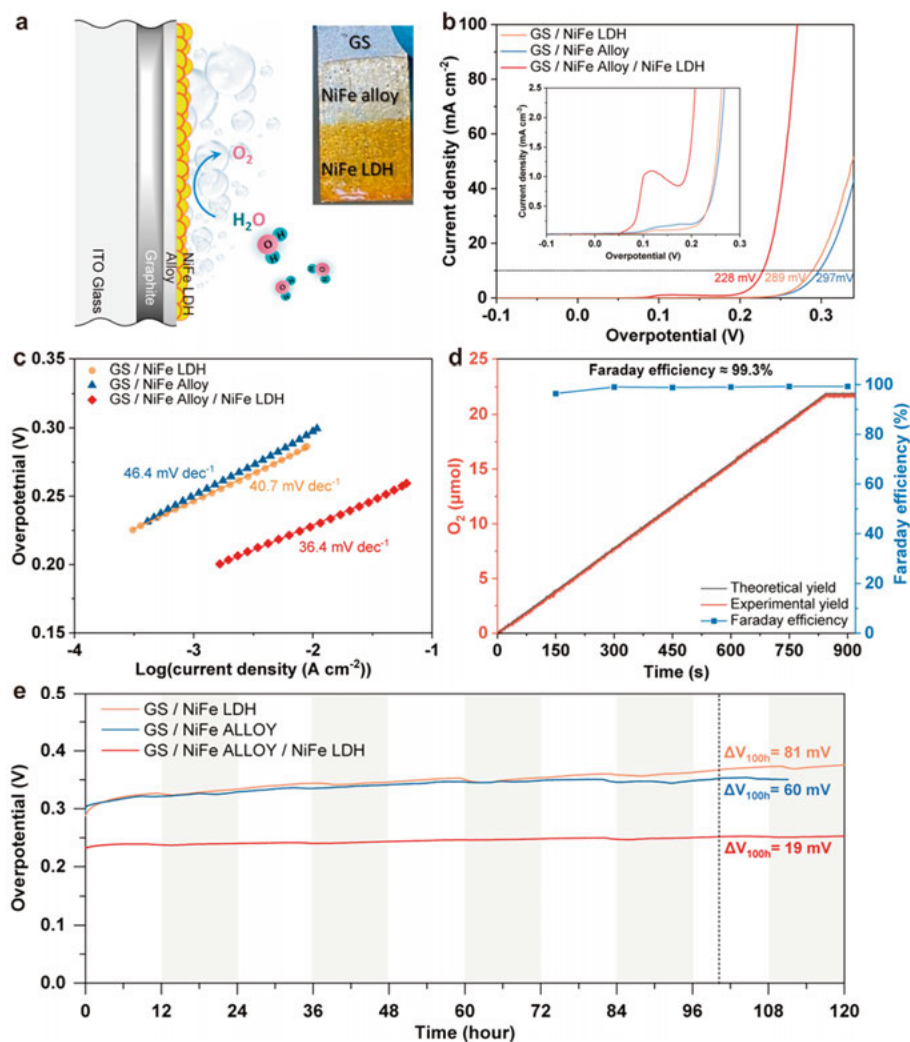


Figure 3-21 (a) Device structure of water oxidation catalyst layer. Inset: digital image of the as-prepared catalyst layer. (b) LSV curves of **GS/NiFe alloy/NiFe LDH**, GS/NiFe alloy, and GS/NiFe LDH in 1.0 M KOH. Inset: LSV curves in $\text{Ni}^{2+}/\text{Ni}^{3+}$ redox region. (c) Corresponding Tafel slopes and (d) Faradaic efficiencies of **GS/NiFe alloy/NiFe LDH** for the OER in 1.0 M KOH. Theoretically calculated and experimentally measured amounts of O_2 were shown as functions of electric charge for water oxidation catalyzed by **GS/NiFe alloy/NiFe LDH** at a current density of 10 mA cm⁻² (electrode area = 1.0 cm²). (e) Chronopotentiometry measurement (10 mA cm⁻²) of **GS/NiFe alloy/NiFe LDH**, GS/NiFe alloy, and GS/NiFe LDH in 1.0 M KOH.

Nickel Iron (NiFe) composition has been widely reported as an efficient electrocatalyst for water oxidation. In our system, a compact attached NiFe alloy layer was first deposited on GS substrate using an electrodeposition method¹¹⁵ to improve the adhesion of the oxides catalyst. Then, active NiFe layer double hydroxide (LDH) was electro-deposited¹¹⁶ onto the GS/NiFe alloy to create a stable and highly active **GS/NiFe alloy/NiFe LDH** part (**Figure 3-21a**). **Figure 3-21b** shows that the **GS/NiFe alloy/NiFe LDH** catalyst exhibits the highest catalytic current compared to the GS/NiFe alloy and GS/NiFe LDH electrodes. Moreover, the overpotential requirement was significantly reduced in the composite **GS/NiFe alloy/NiFe LDH** electrode, with only 228 mV required to reach a current density of 10 mA cm^{-2} , which is 61 and 69 mV lower than that of the GS/NiFe LDH and GS/NiFe alloy electrodes, respectively. **Figure 3-21c** presents the Tafel slopes of the three aforementioned electrodes, which are around 30 to 40 mV dec^{-1} , suggesting the presence of similar active NiFe species on the surface. The inset figure in **Figure 3-21b** displays the linear sweep voltammetry (LSV) curves in the $\text{Ni}^{2+/3+}$ redox region, revealing that the oxidation peak of the **GS/NiFe alloy/NiFe LDH** electrode is significantly larger than that of the GS/NiFe LDH and GS/NiFe alloy electrodes. Thus, the enhanced current observed in the **GS/NiFe alloy/NiFe LDH** electrode is attributed to the higher loading amount of active species. The catalytic stability of the electrodes was evaluated by chronopotentiometry under a constant current density of 10 mA cm^{-2} . As shown in **Figure 3-21e**, **GS/NiFe alloy/ NiFe LDH** electrode exhibits the best stability with only a 19 mV increase in overpotential after 120 hours of catalysis. In contrast, the overpotential increase of the GS/NiFe LDH electrode was 81 mV. The amount of oxygen electrochemically generated from the **GS/NiFe alloy/ NiFe LDH** was confirmed using a pressure transducer. Quantitative yields of 99.3% are obtained under 10 mA cm^{-2} in 1.0 M KOH, respectively, which indicates that accumulated charge is nearly quantitatively consumed in OER (**Figure 3-21d**).

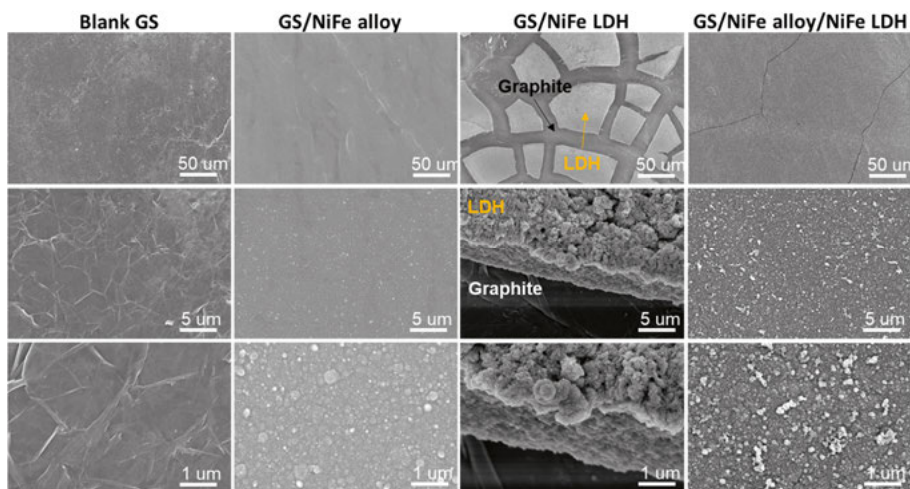


Figure 3-22 SEM images of blank GS, GS/NiFe alloy/NiFe LDH, GS/NiFe alloy, and GS/NiFe LDH under different magnifications

SEM characterized the surface morphology. **Figure 3-22** shows that NiFe alloy could be uniformly deposited onto the graphite layer without clear cracks. However, electroplated NiFe LDH could not form dense layers onto graphite; the isolated NiFe LDH “island” lowered the attach strength and loading amount, leading to poor mechanical strength and catalytic current. After the coating of the alloy layer, a dense NiFe LDH layer could be further obtained by electrodeposition, which makes the GS/NiFe alloy/NiFe LDH electrode the most efficient and stable. The SEM images of electrodes after 120 hours of electrolysis are present in **Figure 3-23**. Most of the NiFe LDH flakes in the GS/NiFe LDH electrode detached, and the graphite layer was exposed, while the NiFe LDH layer in GS/NiFe alloy/NiFe LDH electrode was still closely attached to the substrate despite some cracks being identified.

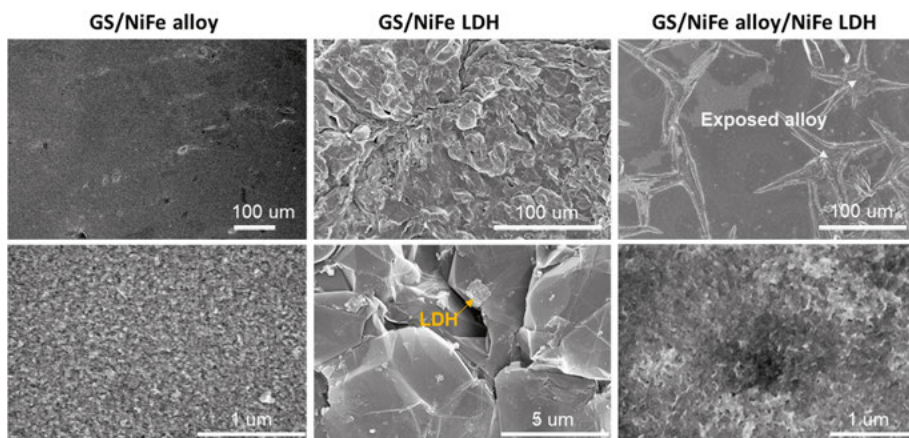


Figure 3-23 SEM images of blank GS, GS/NiFe alloy/NiFe LDH, GS/NiFe alloy, and GS/NiFe LDH after 120 hours' electrolysis.

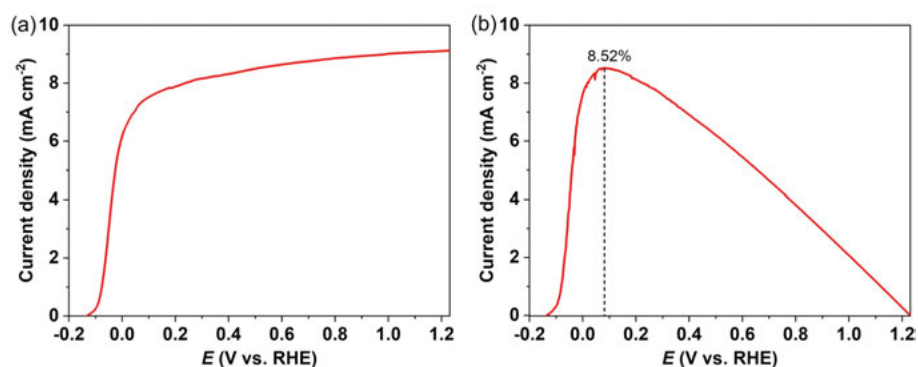


Figure 3-24 (a) LSV curve of FAPbBr₃ photoanode in 1.0 M KOH. (Scan rate: 50 mV s⁻¹). (b) corresponding ABPE calculated from the LSV curve.

In the design structure of ITO/SnO₂/FAPbBr₃/carbon/GS/NiFe alloy/NiFe LDH, the applied bias photon to current efficiencies (ABPEs) was calculated from the corresponding linear sweep voltammetry (LSV) curve in **Figure 3-24**. The maximum ABPE of the FAPbBr₃ photoanode is 8.52 % at 0.082 V vs. RHE. The maximum ABPE value is compared to those previously reported photoanodes, and the results are summarized in **Figure 3-25a**. This value is among the best-reported photoanodes, including a metal oxide, perovskite, polymer bulk heterojunction (BHJ), and silicon-based photoanodes. As light-absorbing materials with similar wide bandgap, the FAPbBr₃ photoanode is far superior to the bismuth vanadate-based photoanodes in terms of maximum ABPE. When considering the ultra-low potential where the maximum ABPE

value lies, the FAPbBr₃ photoanode is one of the most promising candidates for realizing efficient photo-driven total water splitting. **Figure 3-25b** summarizes the best-reported photovoltages for representative PV and PEC devices with corresponding band gaps. Photovoltage of PV devices is presented as the short circuit potential; photovoltage of photoanodes is calculated as the difference between the photocurrent onset potential and the Nernstian potential for water oxidation (1.23 V vs. RHE). Analog to trends of PV devices, a wide bandgap absorber (> 2.0 eV) should be capable of photovoltages approaching >1.4 V when considering free energy losses of 0.6 eV.¹¹⁷ While it is clear that traditional oxide or nitride high bandgap absorbers offer significant potential for improving the photovoltage to reach the goal. To our knowledge, the wide bandgap, HTM-free FAPbBr₃ photoanode in this work has the lowest onset potential (around -0.12 V) and record photovoltage (around 1.35 V) in a single junction photoanode to date. The ultra-low onset potential greatly reduces the counter photocathode requirements, making constructing a low-cost Z-scheme water-splitting system with over 5% solar to hydrogen efficiency more feasible.

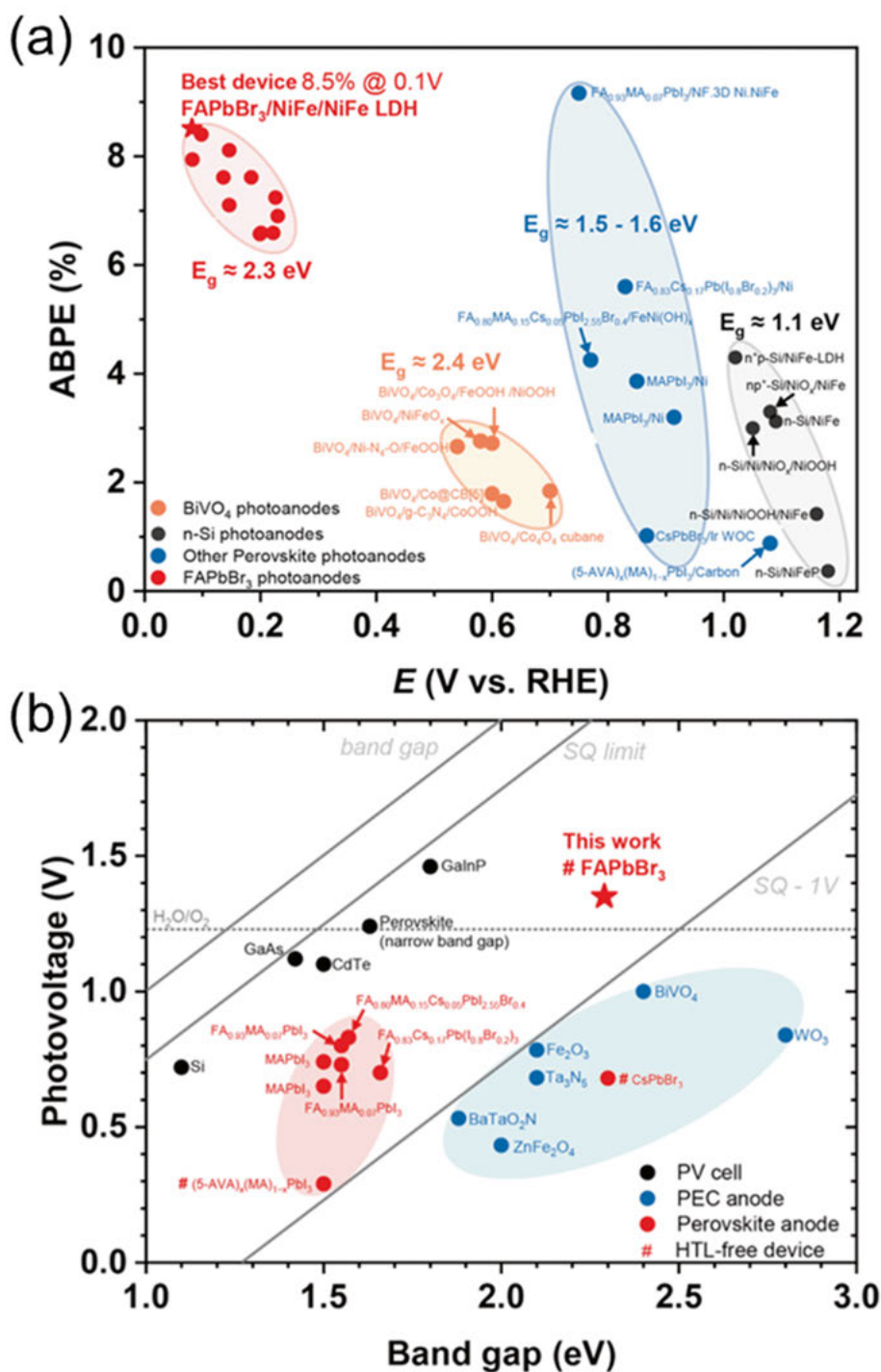


Figure 3-25 (a) ABPE benchmarks of as-prepared FAPbBr₃ photoanodes and other perovskites, BiVO₄, and Si-based photoanodes. (b) Photovoltage

benchmarks for PEC and PV materials as a function of the optical band gap. Diagonal lines represent the band gap, the Shockley-Queisser (S-Q) photo-voltage limit, and the S-Q limit minus 1 V. Tabulated values of PV cell and PEC anodes were retrieved from reference¹¹⁷.

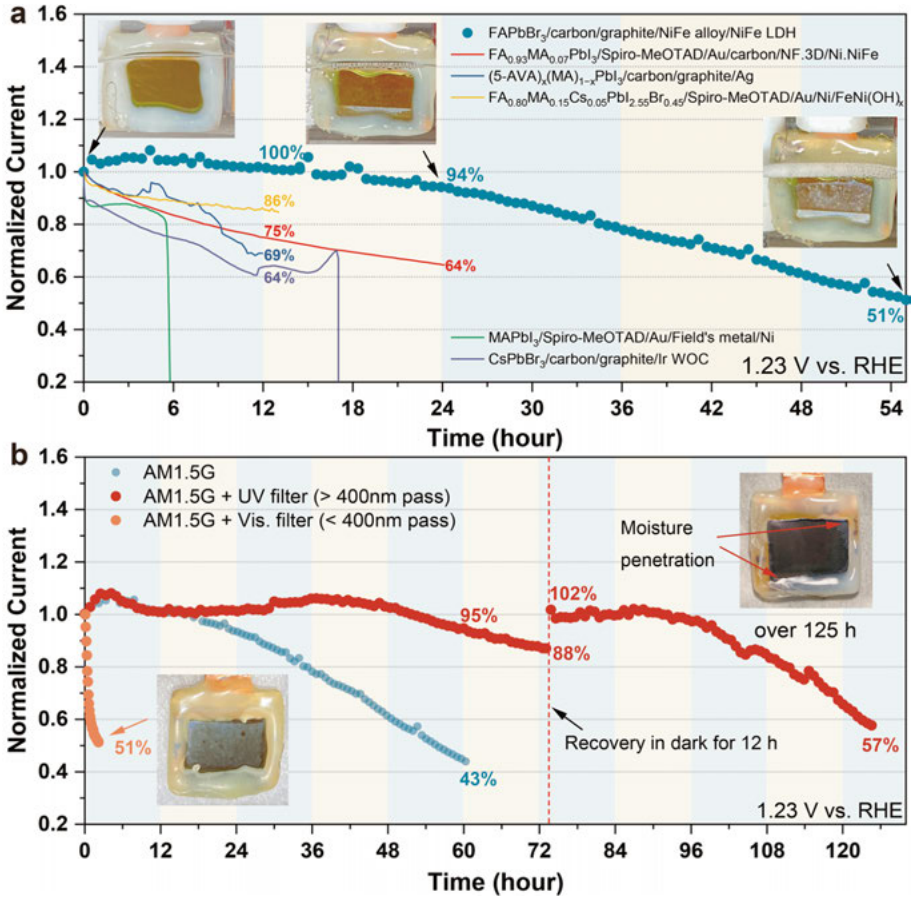


Figure 3-26 (a) Normalized chronoamperometric measurement of FAPbBr₃ photoanode at 1.23 V vs. RHE in 1.0 M KOH solutions (AM 1.5 G, 100 mW cm⁻²). Inset: digital images of photoanode at different light-exposed times. (b) Normalized chronoamperometric measurement of FAPbBr₃ photoanode at 1.23 V vs. RHE with different filters in 1.0 M KOH solutions (AM 1.5G + UV or Vis. filter). Inset: digital images of photoanode at different light-exposed times.

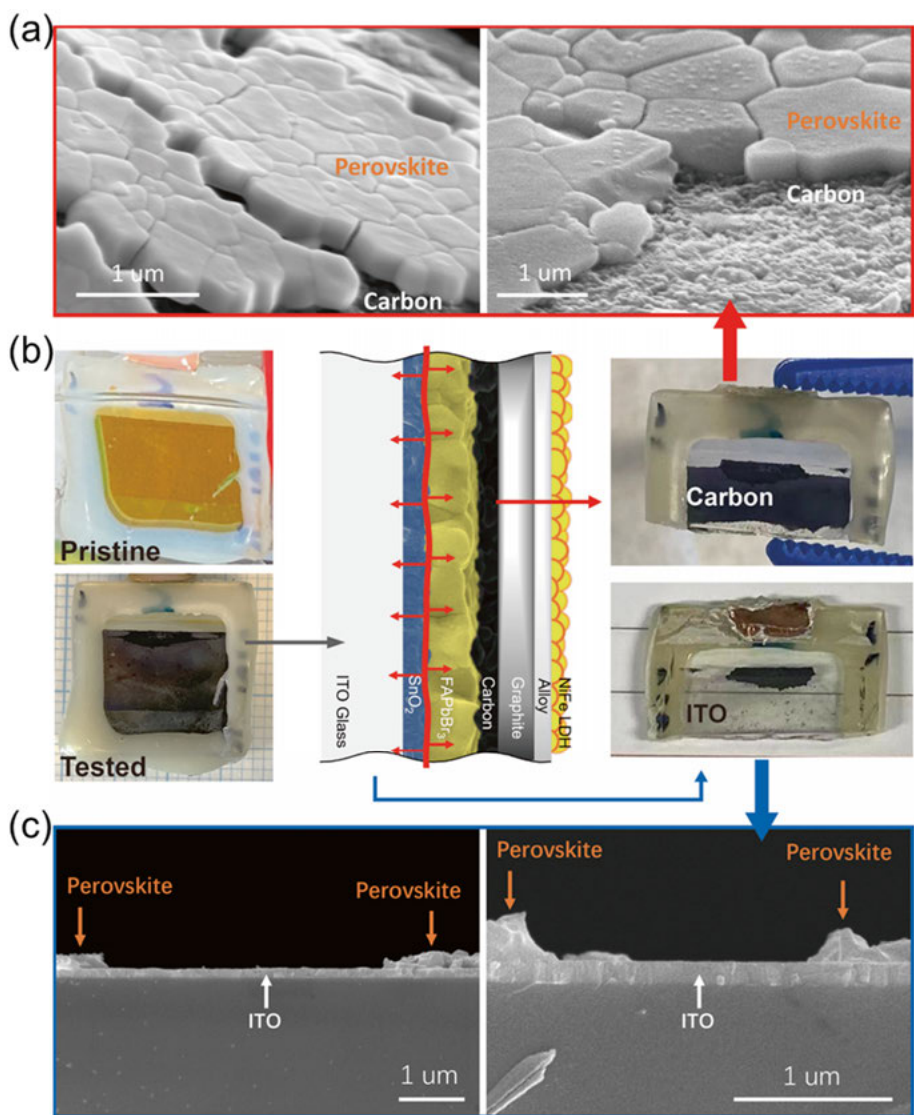


Figure 3-27 (a) SEM images for the carbon part of tested FAPbBr₃ photoanode in oblique view. (b) Schematic diagram of the photoanode degradation process and digital images of pristine and tested FAPbBr₃ photoanode. (c) SEM images for the glass part of tested FAPbBr₃ photoanode in cross-section view.

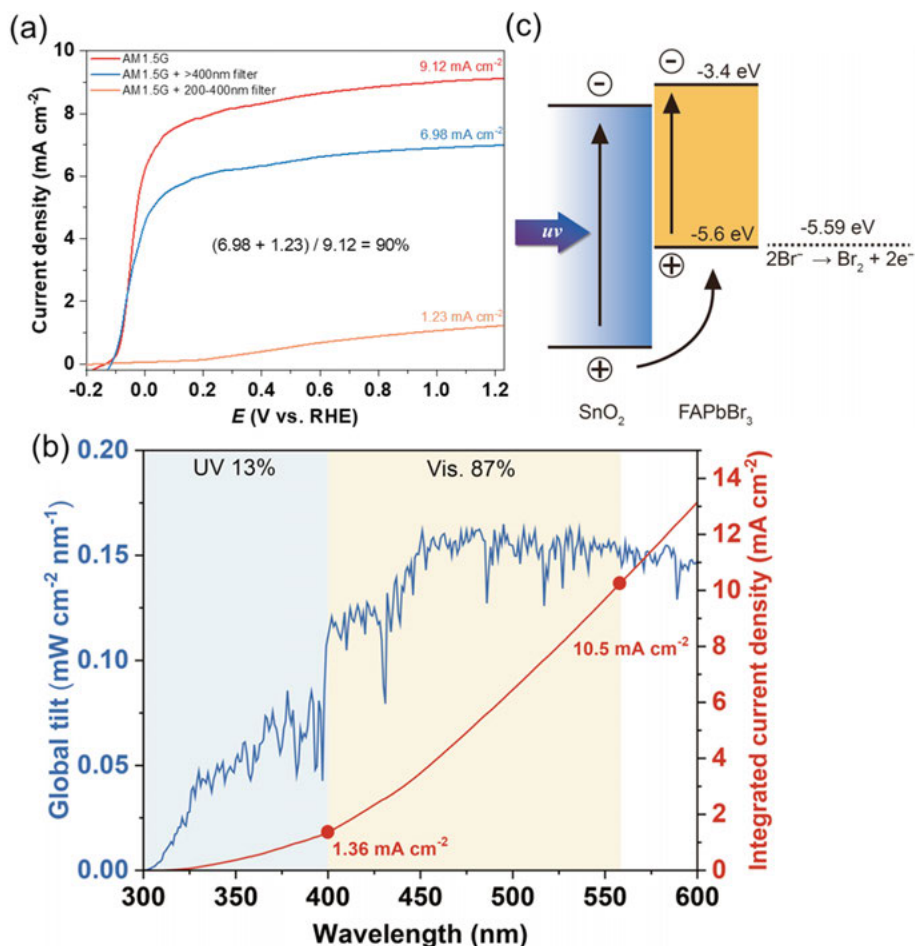


Figure 3-28 (a) LSV curve of FAPbBr₃ photoanode with different filters in 1.0 M KOH (scan rate: 50 mV s⁻¹). (b) AM 1.5G spectrum and corresponding integral current densities for UV (< 400 nm) and maximum absorption edge (< 560 nm) regions. (c) Schematic diagram of the proposed mechanism for UV degradation of FAPbBr₃ photoanode.

Although the NiFe alloy/NiFe LDH-based catalysts and HTM-free FAPbBr₃ solar cells have already shown good stability under operation conditions, achieving long-term stability using integrated photoelectrodes remains challenging to the harsh electrolyte environment of water splitting. To investigate the long-term stability of FAPbBr₃ photoanodes, chronoamperometry with a constant applied potential was conducted in 1.0 M KOH solutions. As shown in **Figure 3-26a**, the initial photocurrent exceeds 8.8 mA cm⁻² under the

applied potential of 1.23 vs. RHE. The device exhibits a half-life of over 55 hours, better than other reported systems in **Figure 3-26a**. Notably, the current shows no decay in the initial 12 hours of illumination and remains at around 95% of its initial current after 24 hours of operation. During the measurement, light-soaking-induced photocurrent enhancement is observed, where the photocurrent gradually increases with the initial 5 hours of illumination.^{58, 118} The stability of the FAPbBr₃ photoanode was also examined under a lower applied potential of 0.3 vs. RHE. The inset images in **Figure 3-26a** show photographs of the PEC cell after 24 and 55 hours of photo-electrolysis. The following investigation aimed to reveal possibilities for improving the stability of degraded photoanodes. To this end, deactivated photoanodes were disassembled to study the degradation mechanism. As shown in **Figure 3-27b**, the tested sample could be easily separated into two parts, with the graphite/carbon layer peeled off from the glass substrate. SEM was employed to observe the interface of the two peeled parts. As shown in **Figure 3-27a**, the perovskite layer tightly adheres to the carbon layer; In contrast, only a small portion of perovskite crystal is attached to the ITO glass substrate (**Figure 3-27c**). For the pristine sample, the ITO glass substrate should be an orange color with the growth of the FAPbBr₃ layer. However, after stability tests, the FAPbBr₃ layer detached from the substrate, resulting in a transparent glass substrate.

The stability of lead halide PSCs is influenced by several factors, including heat, moisture, voltage, and UV light. Among these factors, the stability upon UV light exposure is particularly problematic due to the photocatalytic effect of ETL materials like TiO₂ and SnO₂, which are the main reasons for perovskite degradation.¹¹⁹ In our study, the theoretical oxidation potential of Br⁻ is 1.087 V vs. NHE (pH = 0), which is equivalent to -5.59 eV vs. vacuum level.¹²⁰ Under visible light irradiation, the potential is almost the same as the VBM of perovskite. Thus, self-oxidation is less likely to occur on FAPbBr₃ because the reaction requires a certain additional driving force. However, as indicated in **Figure 3-28c**, charges would accumulate close to the SnO₂/perovskite interface when UV light exposure. These charges could extract electrons from the bromine anion (Br⁻) in the FAPbBr₃ crystals, compromising the perovskite interface structure and producing FAPbBr or PbBr₂. As shown in **Figure 3-28a**, the photocurrent of the FAPbBr₃ photoanode decreased by approximately 25% under UV-filtered light, reducing to about 7.0 mA cm⁻² at 1.23 V vs. RHE. When the cut-off absorption edge is set at 560 nm, the energy of UV light in AM 1.5G spectrum accounted for 13%, delivering a maximum photocurrent density of 1.36 mA cm⁻² (**Figure 3-28b**). When a visible light filter was applied, the photocurrent of the FAPbBr₃ photoanode was limited to 1.23 mA cm⁻² at 1.23 V vs. RHE, and the onset potential dramatically increased under UV light. This observation could be explained by the fact that

UV light cannot penetrate the perovskite film, leading to the insufficient driving force for the carriers to flow to the HTM side. The stability measurements with filtered light are presented in **Figure 3-26b**. It was found that the FAPbBr₃ photoanode degraded rapidly under UV light, with a current half-life of only 2.2 hours, confirming the sensitivity of the perovskite photoanode system to UV light. The color of the FAPbBr₃ layer also turns white, indicating the rapid degradation of the ITO-SnO₂/FAPbBr₃ interface. In contrast, under UV-free illumination, the photoanode is much more stable under operating conditions for 50 hours, retaining almost 100% of the initial photocurrent and gradually decaying to 88% of the initial photocurrent for an additional 24 hours. More importantly, the photocurrent can be restored to the initial level after resting in the dark for 12 hours at open circuit conditions, as commonly observed in regularly structured PSCs with n-i-p architectures.^{121, 122} The system demonstrates remarkable operational stability, with no current decay even after cumulative 96 hours of electrolysis. Eventually, the photocurrent density retains more than 57% of its initial level even after 125 h. As revealed in the inset image in **Figure 3-26b**, the current reduction should be due to a sealing failure in the electrolyte, which led to moisture penetration on the edges. Nevertheless, the center of the perovskite layer does not turn white, indicating its intrinsic stability toward water oxidation catalysis under visible light, implying that further improvements in sealing materials and processes can enhance device stability. To our knowledge, the as-fabricated FAPbBr₃ photoanode is the first lead halide perovskite-based photoanodes with a stability of more than 100 hours to date. Although using a UV filter would cause an additional performance penalty, the saturation current of 7 to 8 mA cm⁻² is still superior to oxide-based photoanodes like BiVO₄ and WO₃, making FAPbBr₃ perovskite a competitive candidate for low-cost photoanode materials.

In conclusion, in the fifth work in this thesis, we successfully fabricated HTL-free-carbon-based FAPbBr₃ with an impressive PCE of 9.16% and outstanding stability without degradation for around one year. This FAPbBr₃-PSC was then applied as a photoanode in a PEC system. The resulting device shows a current density around 8.5 mA cm⁻² at 1.23 V vs. RHE, an onset potential below 0 V vs. RHE, and half-life stability over 55 h using a FAPbBr₃ absorber, a carbon/graphite conductive protection layer and a NiFe alloy/NiFe LDH catalyst in alkaline conditions. Due to the fast catalytic kinetics, high photovoltage, and rational band structure, a high ABPE of 8.5% was reached at 0.08 V vs. RHE. Accordingly, by applying a UV filter, the device achieved record stability of over 100 hours in 1.0 M KOH under constant simulated solar illumination, with currents around 7.5 mA cm⁻² at 1.23 V vs. RHE. In the design structure of ITO/SnO₂/FAPbBr₃/carbon/GS/NiFe alloy/NiFe LDH, the carbon layer serves as both the HTL, while the graphite layer functions as a

waterproof and conductive layer. Meanwhile, the dense electrodeposited alloy layer provides a robust substrate for high-performance LDH catalyst loading while ensuring efficient electrical conductivity. The compact design endows the device with high performance and excellent stability. These observations, along with the ultralow onset potential and the facile processability of FAPbBr₃ photoanode, demonstrate the potential of lead halide perovskite-based PEC as a promising approach to achieving efficient, cost-effective, and scalable photoelectrochemical solar fuel production.

Conclusions and Outlook

PSCs represent a new photovoltaic technology that holds great promise for low-cost light conversion to electricity. Bromide-based wide-bandgap perovskites are especially useful as the top cell in a tandem device and for light-assisted water splitting, potentially facilitating a low-carbon society. However, the efficiency of PSCs based on bromide is decreased by substantial V_{oc} and FF losses, representing the main obstacle to their photovoltaic performance. Nonradiative recombination and band alignment mismatch between the perovskite and transport layers constitute the principal energy loss channels, contributing to the V_{oc} loss and significant PCE losses. Furthermore, the extensive adoption of PSCs is impeded by a lack of long-term stability partly due to the employment of inefficient, unstable, complicated, and expensive charge transport materials. Therefore, optimizing charge transport, reducing losses, and employing stable HTM is critical to guarantee the durability and longevity necessary for advancing emerging solar cells closer to mass production and their applications in water splitting and tandem devices. High perovskite crystallinity quality is crucial in reducing perovskite defects and suppressing non-radiative recombination processes. Of the various recombination processes, defect-induced recombination is the important contributor to the reduced FF and V_{oc} . This thesis presents a series of approaches to prepare high-quality FAPbBr₃ perovskite, reduce interface defects, investigate different HTMs, and replace the gold contact with a carbon electrode to increase performance and reduce the cost of FAPbBr₃-based devices.

The production of a high-quality perovskite layer is a critical factor in achieving high-performance PSCs. Accordingly, **Paper I** and **Paper II** presented in this thesis were dedicated to the engineering and preparation of the perovskite layer. Specifically, in **Paper I**, MABr, and MACl additives in the FABr solution were employed to increase the crystal size and perovskite film crystallinity, which improved the photovoltage performance. Meanwhile, **Paper II** employed a mixed solvent approach in the second step of the fabrication process, which led to favourable characteristics such as high-quality crystallization, suitable solubility, large grain size, and improved charge extraction properties.

The presence of defects on the grain boundaries or surface is a major hindrance to the performance of devices. In **Paper III**, an ultrathin 2D perovskite layer

of (PEA)₂PbBr₄ was applied to the 3D perovskite of FAPbBr₃, resulting in a significant reduction in defect density and improvement in interfacial charge extraction efficiency. This, in turn, led to a marked enhancement of PCE from 7.7% to 9.4% and FF from 67.6% to 77.6%.

Paper I-III employed Spiro-OMeTAD doped with additives as an HTM in PSCs, a commonly utilized HTM. However, due to its hydrophilic nature and ion migration, using additives in Spiro-OMeTAD has led to device instability and degradation. **Paper II** demonstrated that dopant-containing Spiro-OMeTAD-based FAPbBr₃-PSCs were unstable in ambient environments due to its hydrophilic nature and ion migration, resulting in numerous pinholes on the sample surface. **In Paper IV**, four dopant-free HTMs were evaluated on FAPbBr₃-PSCs based on their structure-property relationship. P3HT, one of the evaluated HTMs, displayed higher hole mobility, resulting in superior charge extraction and transport. The optimized P3HT-based device displayed a V_{oc} of 1.47 V and a champion efficiency of 9.4%, with improved operational stability, making it one of the highest-performing FAPbBr₃-PSCs based on dopant-free HTMs. However, despite the improved stability, the efficiency of dopant-free P3HT devices still declined by 40% after four months, indicating the need for further stability enhancements.

In **paper V**, an HTL-free- FAPbBr₃ device with a carbon electrode was successfully fabricated with an impressive PCE of 9.16% and outstanding stability without degradation for around one year. This structure was then applied as a photoanode in the PEC system. It demonstrated a FAPbBr₃ photoanode featuring a current density around 8.5 mA cm⁻² at 1.23 V vs. RHE, an onset potential below 0 V vs. RHE, and half-life stability over 55 h using a FAPbBr₃ absorber, a carbon/graphite conductive protection layer, and a NiFe alloy/NiFe LDH catalyst in alkaline conditions. Further stability studies and post-characterizations revealed that the perovskite interface was damaged by UV light, resulting in a detached absorber layer and performance loss. Accordingly, by applying a UV filter, the device achieved record stability of over 100 hours in 1.0 M KOH under constant simulated solar illumination, with currents around 7.5 mA cm⁻² at 1.23 V vs. RHE. The compact and efficient design of the photoanode contributes to its excellent stability and high performance. These findings, combined with the facile processability and ultralow onset potential of FAPbBr₃ PEC photoanodes, indicate their potential for practical and scalable photoelectrochemical solar fuel production.

Despite making progress in enhancing the performance and stability of FAPbBr₃-based PSCs through our investigation into these five projects, the issue of voltage losses in PV devices based on FAPbBr₃ persists and needs to be addressed to further promote the application of this type of PSC in the future.

The primary cause of this challenge is the mismatched energy levels between SnO_2 and FAPbBr_3 , as demonstrated in **Figure 1-4**. As a result, finding an ideal ETL for FAPbBr_3 -PV devices is crucial to achieving the maximum V_{oc} for Br-based perovskite devices. According to Arava et al., an ideal ETL material for Br-based perovskite devices should have a CBM situated 3.1 eV below the vacuum level, an energy gap exceeding 3 eV, and E_{Fermi} lower than 100 meV below the CBM.¹²³ These requirements are necessary to maintain the ETL selectivity while preventing voltage losses through electron transfer. Passivating the SnO_2 interface is also a promising approach to reducing energy loss during electron transfer, as confirmed in other PSCs. To achieve this, organic compounds with mixed charged functional groups, such as self-assembled monolayers and zwitterionic organic compounds, have been used to bond the SnO_2 layer to the perovskite layer passivate SnO_2 with superior interfacial optoelectronic properties.¹²⁴ Therefore, further research on the ETL side should be considered as a potential avenue for pushing the voltage of bromine-based PSCs close to the S-Q limit.

Acknowledgments

First and foremost, I would like to express my sincere gratitude to my dear supervisor, **Prof. Erik M. J. Johansson**, who offered me this great opportunity to start my Ph.D. in a wonderful group and led me to an interesting and promising research field. I will never forget the period before I received your offer. It was the darkest period of my life. Thank you for allowing me to overcome that dark time. It is no exaggeration to say you changed my life routine and brought sunshine to a girl in the darkness. I am very grateful to have been your student. From the first interview to the email telling me I had been accepted, to joining your research group, starting my project, and now writing my thesis, I have felt your unwavering support and encouragement every step of the way. You have given me ample resources and practical feedback, given me the trust and freedom to conduct my research, and shown me endless equality and respect. Thank you for the tremendous honor of being your Ph.D. student. I truly appreciate everything you have done for me. You are the best supervisor in the world.

I would then really want to thank my lab brothers, Dr. **Byeong Jo Kim** and Dr. **Bin Cai**. To **Kim**, I am so grateful for your endless help at the beginning of my Ph.D. study. You tried (of course, failed) to train me to be a perfect solar celler like you. Thank you very much for encouraging and always helping me, which initially made my doctoral projects smooth. To **Bin**, I can say that you were very helpful to me during the second half of my Ph.D. study. At that time, I had just met the bottleneck of the project. I made no progress in the experiment for over a year and suffered physical and mental damage. Thank you for always encouraging and telling me this is a normal situation in a Ph.D. life. Thank you for using your experience to help me find the problems in my experiments, help me optimize the conditions, and finally finish my projects.

To my co-supervisor **Prof. Gerrit Boschloo**. I am grateful for the opportunity to study in our group under your guidance. Your knowledgeable speeches and scientific insights have been a valuable source of learning for me. I am also grateful for your assistance in revising my study plans and papers, which has been extremely helpful. To our lab engineer **Dr. Leif Häggman**, thank you very much for your hard work in managing the laboratory and always

providing timely help for my work, which has allowed my work to run smoothly. To **Prof. Leif Hammarström**, I am proud to be a Ph.D. student in the physical chemistry department under your supervision. I am grateful for your assistance in revising my study plans and organizing many useful Ph.D. student meetings. Your rigorous attitude toward scientific research, fairness, wisdom, and charisma impressed me. You are the best role model I have encountered during my doctoral studies.

To my most wonderful BaGua group, Huimin, Hua, Aijie, Heyin, Yanni (Catherine), Zhen (Jenny), Minli, Fangwen, Andjela Brnovic, Jing Fang, Dr. Bitao Dong, Dr. Hongwei Song, Xinjian Geng, Sicong Wang, Dr. Chen Ye, Dr. Xianshao Zou, Dr. Haoliang Cheng, Dr. Jingguo Li, Zhanwei Yu, Dr. Fuxiang Ji and Dr. Min Tao. I am so lucky to have met you guys in Uppsala. Thank you, guys, for giving me a lot of happiness, always supporting me, patiently listening to my negative conversation, and encouraging me to overcome my anxiety. You are my most treasured memory in Sweden.

My lovely group colleagues Dr. Malin Johansson, Dr. Fuxiang Ji, Aneta Andruszkiewicz, Dr. Lin Yuan, Fiona Treber, Dr. Hannes Michaels, Dr. Soe Ko Ko Aung, Dr. Vishnu Vijayakumar, Anuja Vijayan, Bhavya Rakheja, Rajarshi Roy, Dr. Honglin Yu, and Dr. Shipra Prakash. I am so happy to work with you guys. You guys build such a lovely group. I wish all of you the best.

For other colleagues in our department, Prof. Haining Tian, Prof. Starla Glover, Prof. Reiner Lomoth, Prof. Jacinto Sá, Princess Cabotaje, Robert Bericat Vadell, Vitor Silveira, Dr. Gaurav Kumar, Dr. Yocef Hattori, Nidhi Kaul, Qixiao He and all others in our department. Thank you all for the discussions, meetings, and parties.

Other friends in Sweden: Dr. Pei Fu, Yingtao Yu, Zunyuan Zheng, Xueying Kong, Yu Bai, Dr. Shengyang Zhou, Dr. Huang Wang, and all the youth group friends in Uppsala. It has been a pleasure to meet you guys in Uppsala. Also, I thank Fan Zhang and Fan Yang for bringing my lovely cats babies into the world and letting them join my family.

Many thanks to the Licheng Sun group, Prof. Licheng Sun, Dr. Linqin Wang, Dr. Qijun Meng, Dr. Tianqi Liu, and Dr. Fuguo Zhang. I am especially grateful to Prof. Licheng Sun for inviting me to visit Westlake University. I learned a lot and ate the most delicious Hangzhou food. It was a very enjoyable time.

Thanks for the financial support from the traveling scholarships of Liljewalch and Thelins G scholarship.

Other friends in China. Tui (Tao Chen), I am always grateful for your help during my darkest time in South Korea. I am so happy you have found your

dream job now. Then my friends in Nanchang, my lovely couple of Shiyang and Qiu, and my not-so-frequently-in-contact friend Cheng Xiong. When I wrote this thesis, I always remembered our time together during our youth. We've been best friends since we were teenagers, and I have always remembered you guys saying that when I finish my Ph.D., you hope your names will be on my thesis, so it would be as if you're always here for me. Thank you for your help and encouragement over the years. Then thank lab brother Xiaotian Hu for always kindness help me during my master's and Ph.D. study and Xiangchuan Meng for sharing many useful experiment tips. Also, Bro Lin Zhang gave me a lot of encouragement during my study overseas. Thanks a lot for your gays.

Then, my home girl, Chenjie, my cutest girl in the world, even though you dream of being the sexiest, most mature girl, you are still cute, just as you were four years ago. I am very grateful to have met you in Sweden. During the four years in Sweden, we could always talk to, encourage, and witness each other's growth. I always feel like you are my family sister in Sweden. My girl, you deserve the best in the world.

最后，我永远感谢爷爷奶奶，爸爸妈妈，弟弟妹妹们对我的支持。然后感谢杨爸杨妈，非常开心和你们组成新的一家人。最后，感谢世界上最好的伴侣，我的昊哥。你是我在这个世界上最喜欢的人。其他的不多说。还有就是我的猪猪跟我的小兰，很开心你们加入我们的小家庭。

Popular science summary

The phenomenon of global warming, also known as the greenhouse effect, occurs when certain gases in the Earth's atmosphere trap heat, leading to a gradual increase in the planet's temperature. Human activities, such as burning fossil fuels, emit greenhouse gases like carbon dioxide, which primarily cause this effect. With the increasing impact of global climate change, the need for renewable energy sources is urgent. Energy is crucial for human society, and the development of sustainable energy sources is vital both due to environmental reasons, as stated above, and since conventional energy sources continue to deplete.

Solar energy utilization is a promising prospect among the alternative energy solutions being investigated because of its abundant potential and eco-friendliness. A proficient approach to harnessing solar power is through the use of photovoltaic devices that transform solar energy into electricity. This method is known as the photovoltaic effect, which converts photons (light) into voltage and current (electricity). Nowadays, solar cells are becoming increasingly cost-competitive in numerous regions, and large-scale photovoltaic systems are being implemented to aid in the generation of electricity for the power grid. Silicon solar cells were the first to enter industrial production and can achieve a photoelectric conversion efficiency of 27.6%. Thin film solar cells were the second generation, and followed by the third generation of solar cells requires further development to increase efficiency.

Perovskite solar cells have emerged as promising solar cells. They use a metal-halide perovskite as the light-absorbing layer and can be cheaper and easier to manufacture while still achieving high levels of efficiency in converting sunlight into electricity. Perovskite solar cells have many advantages, including their versatility in colour and shape and their potential to be incorporated into building materials for energy-efficient buildings.

Despite these advantages, perovskite solar cells still face technical challenges with stability and efficiency. There are various kinds of perovskite materials, the bromide-based wide-bandgap perovskites (such as FAPbBr_3) are especially useful as the top cell in a tandem device and for light-assisted water splitting, potentially facilitating a low-carbon society. However, the efficiency

of PSCs based on bromide is decreased by substantial V_{oc} losses, representing the main obstacle to their photovoltaic performance. It is critical to guarantee the durability and longevity necessary for advancing emerging solar cells closer to mass production and application in water splitting and tandem devices. This is where my thesis comes in.

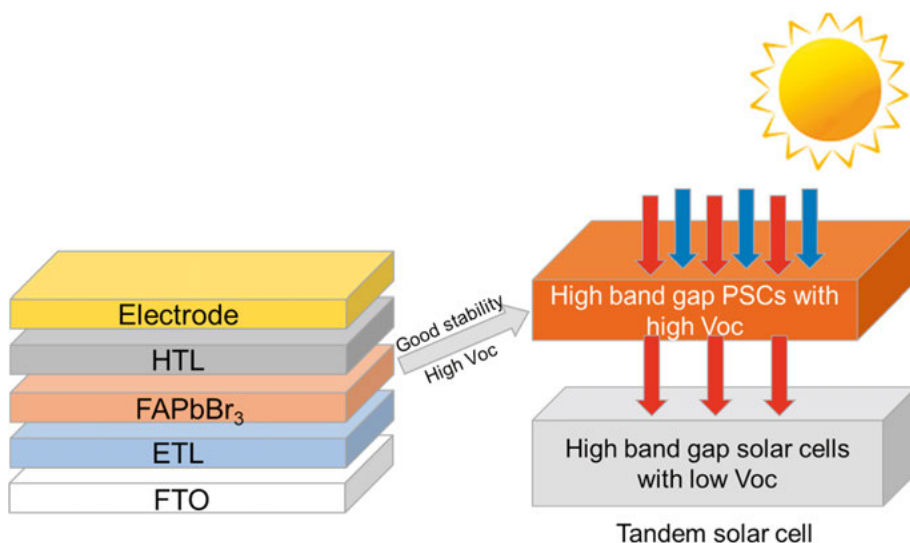


Figure 4-1 Solar PV.

This thesis presents five works that explore different methods to improve the performance and stability of FAPbBr₃-based PSCs. The first work demonstrates using MABr and MACl additives to enhance crystal size and film crystallinity, improving photovoltage performance. The second work investigates using mixed solvents and adding MACl to enhance PSC performance further. The third work focuses on passivating interface defects using a 2D perovskite layer, improving photovoltaic performance and stability. The fourth work explores using different dopant-free hole transport materials, with P3HT showing the best performance and stability. Finally, the fifth work presents a novel approach to FAPbBr₃-based PSCs using an HTL-free carbon-based structure as a photoanode in a photoelectrochemical solar fuel production system, achieving impressive efficiency and stability.

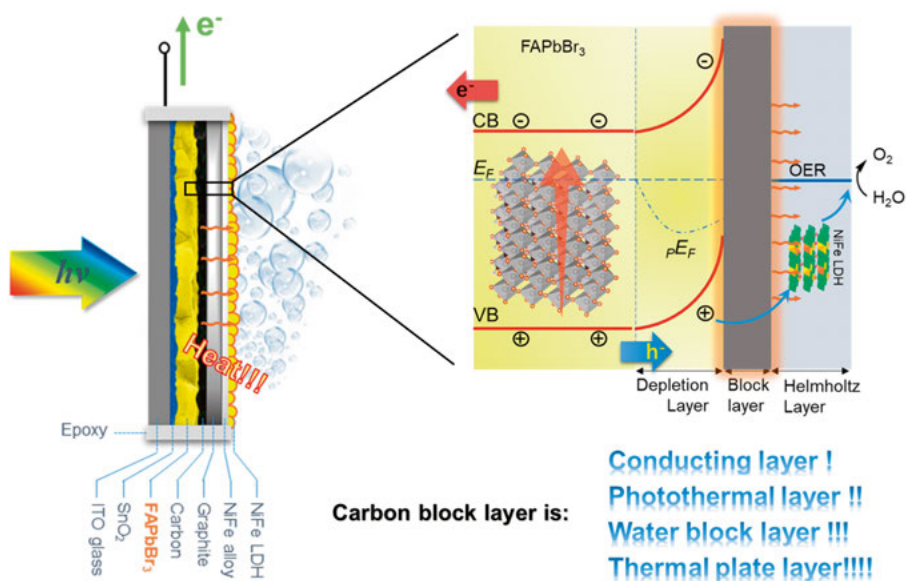


Figure 4-2 PSCs as photoanode in a photoelectrochemical solar fuel production system.

In conclusion, the works presented in this thesis show the promising potential of lead halide perovskite-based PSCs for achieving efficient, cost-effective, and scalable solar energy production. Through various methods explored in this thesis, solutions are proposed to enhance the performance and stability of PSCs. The results suggest that the high bandgap FAPbBr₃ perovskite material holds high potential for applications in solar and photoelectrochemical cells.

Populärvetenskaplig sammanfattning

Fenomenet global uppvärmning, även känt som växthuseffekten, uppstår när vissa gaser i jordens atmosfär fångar värme och leder till en gradvis ökning av planetens temperatur. Mänskliga aktiviteter, som att bränna fossila bränslen, avger växthusgaser som koldioxid, vilket främst orsakar detta. Med den ökande påverkan av global klimatförändring är behovet av förnybara energikällor brådskande. Energi är avgörande för det mänskliga samhället, och utvecklingen av hållbara energikällor är avgörande dels pga miljöeffekterna beskrivna ovan och eftersom konventionella energireserver fortsätter att minska.

Ett bra tillvägagångssätt för att utnyttja solenergi är genom användning av solceller som omvandlar solenergi till elektricitet. Denna metod är känd som den fotovoltaiska effekten, som omvandlar fotoner (ljus) till spänning och ström (elektricitet). Nuförtiden blir solceller alltmer kostnadskonkurrenskraftiga i många regioner, och storskaliga fotovoltaiska system implementeras för att hjälpa till att generera elektricitet till elnätet. Kisel-solceller var de första som gick in i industriell produktion och kan uppnå en fotoelektrisk omvandlingseffektivitet på 27,6 %. Tunnfilmssolceller var andra generationen, och följt av tredje generationens solceller kräver vidareutveckling för att öka effektiviteten.

Perovskit solceller (PSCs) har nyligen dykt upp som lovande solceller. De innehåller metal-halid perovskit som ljusabsorberande skikt och kan vara billigare och enklare att tillverka samtidigt som de uppnår höga nivåer av effektivitet i omvandling av solljus till elektricitet. Perovskit-solceller har många fördelar, inklusive deras mångsidighet i färg och deras potential att integreras i byggnadsmaterial för energieffektiva byggnader.

Trots dessa fördelar står perovskit-solceller fortfarande inför tekniska utmaningar med stabilitet och effektivitet. Det finns olika typer av perovskitmaterial, där bromidbaserade bredbandgap-perovskiter (som FAPbBr_3) är särskilt användbara som toppcell i en tandem-enhet och för ljusassisterad vattensplittring, vilket potentiellt underlättar ett framtida lågkolssamhälle. Effektiviteten för PSCs baserade på bromid begränsas dock av betydande spänningsförluster, vilket representerar den största begränsningen för deras fotovoltaiska prestanda. Det är också avgörande att garantera en hållbarhet och livslängd som krävs för att avancera nya solceller närmare massproduktion för

tillämpning i vattensplittring och tandem-enheter. Det är här min avhandling kommer in.

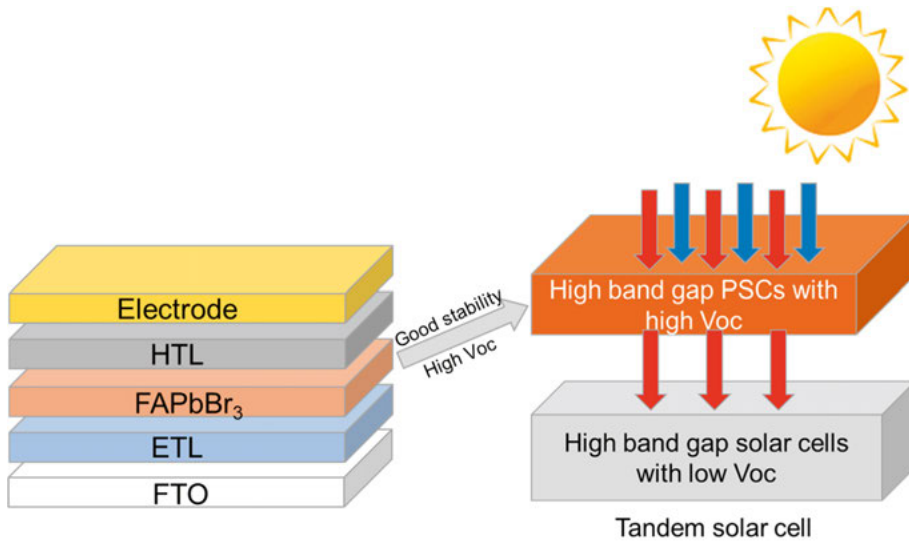


Bild 4-1 Solenergi PV.

Denna avhandling presenterar fem arbeten som utforskar olika metoder för att förbättra prestanda och stabilitet hos PSC:er baserade på FAPbBr₃. Det första arbetet demonstrerar användningen av MABr- och MACl-tillsatser för att förbättra kristallstorlek och filmkristallinitet, vilket förbättrar solcellsprestanda. Det andra arbetet undersöker användning av blandade lösningsmedel och tillsats av MACl för att ytterligare förbättra prestanda. Det tredje arbetet fokuserar på passivering av gränssnittsdefekter med hjälp av ett 2D-perovskitlager, vilket förbättrar fotovoltaisk prestanda och stabilitet. Det fjärde arbetet utforskar användning av olika dopningsfria håltransportmaterial, där P3HT ger bäst prestanda och stabilitet. Slutligen presenterar det femte arbetet ett nytt tillvägagångssätt för att använda FAPbBr₃-baserade PSC:er tillsammans med en HTL-fri kolbaserad struktur som fotoanod i ett fotoelektrokemiskt solbränsleproduktionssystem, vilket uppnår imponerande effektivitet och stabilitet.

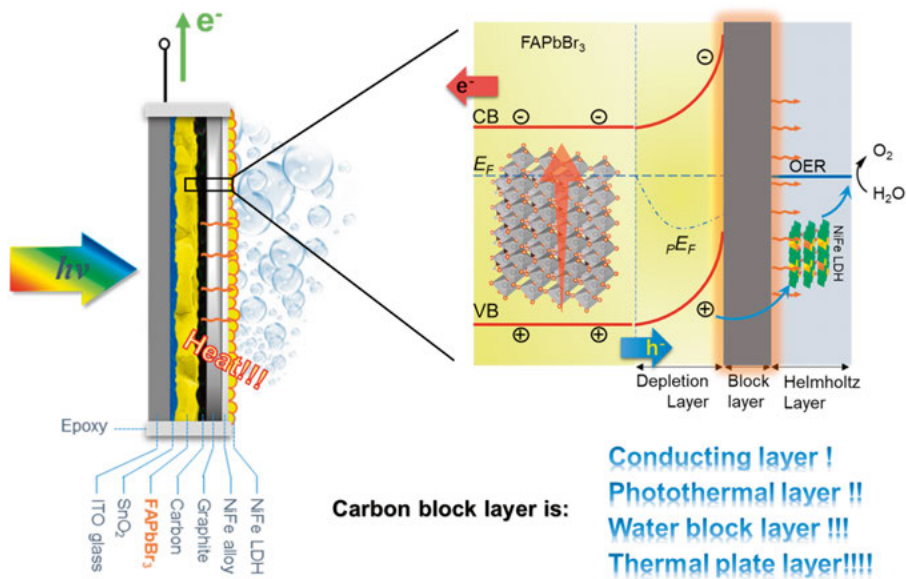


Bild 4-2 PSC:er som fotoanod i ett fotoelektrokemiskt solbränsleproduktions-system.

Slutsatsen från arbetena som presenteras i denna avhandling visar lovande potential för PSC:er baserade på hög bandgaps-perovskit att uppnå effektiv, kostnadseffektiv och skalbar solenergiproduktion. Genom olika metoder som utforskas i denna avhandling föreslås lösningar för att förbättra prestanda och stabilitet hos PSC:er. Resultaten tyder på att högbandgap-perovskitmaterialet FAPbBr_3 har stor potential för tillämpningar inom sol- och fotoelektrokemiska celler.

Reference

1. Y. Liu, B. J. Kim, H. Wu, L. Yuan, H. Zhu, A. Liu and E. M. J. Johansson, *ACS Applied Energy Materials*, 2020, **3**, 9817-9823.
2. Y. Liu, B. J. Kim, H. Wu, G. Boschloo and E. M. J. Johansson, *ACS Applied Energy Materials*, 2021, **4**, 9276-9282.
3. M. Becquerel, *Comptes rendus hebdomadaires des séances de l'Académie des sciences*, 1839, **9**, 561-567.
4. Y. R. Smith and P. Bogust, Cham, 2018.
5. O. O. Ogbomo, E. H. Amalu, N. N. Ekere and P. O. Olagbegi, *Renewable and Sustainable Energy Reviews*, 2017, **75**, 1225-1238.
6. <https://www.nrel.gov/pv/cell-efficiency.html>.
7. T. D. Lee and A. U. Ebong, *Renewable and Sustainable Energy Reviews*, 2017, **70**, 1286-1297.
8. V. M. Goldschmidt, *Naturwissenschaften*, 1926, **14**, 477-485.
9. M. M. Lee, J. Teuscher, T. Miyasaka, T. N. Murakami and H. J. Snaith, *Science*, 2012, **338**, 643-647.
10. A. Kojima, K. Teshima, Y. Shirai and T. Miyasaka, *Journal of the American Chemical Society*, 2009, **131**, 6050-6051.
11. F. Xie, C.-C. Chen, Y. Wu, X. Li, M. Cai, X. Liu, X. Yang and L. Han, *Energy & Environmental Science*, 2017, **10**, 1942-1949.
12. M. Saliba, T. Matsui, J.-Y. Seo, K. Domanski, J.-P. Correa-Baena, M. K. Nazeeruddin, S. M. Zakeeruddin, W. Tress, A. Abate, A. Hagfeldt and M. Grätzel, *Energy & Environmental Science*, 2016, **9**, 1989-1997.
13. D. Weber, *Zeitschrift für Naturforschung B*, 1978, **33**, 1443-1445.
14. D. Weber, *Zeitschrift für Naturforschung B*, 1978, **33**, 862-865.
15. H. S. Jung and N. G. Park, *Small*, 2015, **11**, 10-25.
16. X. Zhu, Z. Xu, S. Zuo, J. Feng, Z. Wang, X. Zhang, K. Zhao, J. Zhang, H. Liu, S. Priya, S. F. Liu and D. Yang, *Energy & Environmental Science*, 2018, DOI: 10.1039/C8EE02284D.
17. H. Huang, B. Pradhan, J. Hofkens, M. B. J. Roelofs and J. A. Steele, *ACS Energy Lett.*, 2020, **5**, 1107-1123.
18. K. Choi, H. Choi, J. Min, T. Kim, D. Kim, S. Y. Son, G.-W. Kim, J. Choi and T. Park, *Solar RRL*, 2020, **4**, 1900251.
19. A. K. Jena, A. Kulkarni and T. Miyasaka, *Chemical Reviews*, 2019, **119**, 3036-3103.

20. D. B. Mitzi, in *Progress in Inorganic Chemistry*, 1999, DOI: <https://doi.org/10.1002/9780470166499.ch1>, pp. 1-121.
21. A. Amat, E. Mosconi, E. Ronca, C. Quarti, P. Umari, M. K. Nazeeruddin, M. Grätzel and F. De Angelis, *Nano Letters*, 2014, **14**, 3608-3616.
22. R. D. Shannon, *Acta crystallographica section A: crystal physics, diffraction, theoretical and general crystallography*, 1976, **32**, 751-767.
23. C. Randall, A. Bhalla, T. Shrout and L. Cross, *Journal of Materials Research*, 1990, **5**, 829-834.
24. A. T. R. Simon, *Journal of Physics: Condensed Matter*, 1996, **8**, 8267.
25. Y. Zhao and K. Zhu, *The Journal of Physical Chemistry C*, 2014, **118**, 9412-9418.
26. T. Leijtens, B. Lauber, G. E. Eperon, S. D. Stranks and H. J. Snaith, *The journal of physical chemistry letters*, 2014, **5**, 1096-1102.
27. A. Dualeh, N. Tétreault, T. Moehl, P. Gao, M. K. Nazeeruddin and M. Grätzel, *Advanced Functional Materials*, 2014, **24**, 3250-3258.
28. N. J. Jeon, J. H. Noh, Y. C. Kim, W. S. Yang, S. Ryu and S. I. Seok, *Nature materials*, 2014, **13**, 897-903.
29. L. Etgar, P. Gao, Z. Xue, Q. Peng, A. K. Chandiran, B. Liu, M. K. Nazeeruddin and M. Grätzel, *Journal of the American Chemical Society*, 2012, **134**, 17396-17399.
30. M. H. Kumar, N. Yantara, S. Dharani, M. Graetzel, S. Mhaisalkar, P. P. Boix and N. Mathews, *Chemical Communications*, 2013, **49**, 11089-11091.
31. H. Min, D. Y. Lee, J. Kim, G. Kim, K. S. Lee, J. Kim, M. J. Paik, Y. K. Kim, K. S. Kim, M. G. Kim, T. J. Shin and S. Il Seok, *Nature*, 2021, **598**, 444-450.
32. L. Zhang, X. Zhang, X. Xu, J. Tang, J. Wu and Z. Lan, *Energy Technology*, 2017, **5**, 1887-1894.
33. W. S. Yang, B.-W. Park, E. H. Jung, N. J. Jeon, Y. C. Kim, D. U. Lee, S. S. Shin, J. Seo, E. K. Kim, J. H. Noh and S. I. Seok, *Science*, 2017, **356**, 1376-1379.
34. Y. Zheng, X. Yang, R. Su, P. Wu, Q. Gong and R. Zhu, *Advanced Functional Materials*, 2020, **30**, 2000457.
35. J. M. Ball and A. Petrozza, *Nature Energy*, 2016, **1**, 16149.
36. D. Yang, R. Yang, K. Wang, C. Wu, X. Zhu, J. Feng, X. Ren, G. Fang, S. Priya and S. Liu, *Nature Communications*, 2018, **9**, 3239.
37. D. H. Kim, J. B. Whitaker, Z. Li, M. F. A. M. van Hest and K. Zhu, *Joule*, 2018, **2**, 1437-1451.
38. Y.-S. Chou, L.-H. Chou, A.-Z. Guo, X.-F. Wang, I. Osaka, C.-G. Wu and C.-L. Liu, *ACS Sustainable Chemistry & Engineering*, 2019, **7**, 14217-14224.
39. Z. Wang, Q. Lin, F. P. Chmiel, N. Sakai, L. M. Herz and H. J. Snaith, *Nature Energy*, 2017, **2**, 17135.

40. G. Grancini, C. Roldán-Carmona, I. Zimmermann, E. Mosconi, X. Lee, D. Martineau, S. Narbey, F. Oswald, F. De Angelis, M. Graetzel and M. K. Nazeeruddin, *Nature Communications*, 2017, **8**, 15684.
41. T. H. Schloemer, J. A. Christians, J. M. Luther and A. Sellinger, *Chemical Science*, 2019, **10**, 1904-1935.
42. J. Yang and T. L. Kelly, *Inorganic Chemistry*, 2017, **56**, 92-101.
43. D. Bryant, N. Aristidou, S. Pont, I. Sanchez-Molina, T. Chotchunangatchaval, S. Wheeler, J. R. Durrant and S. A. Haque, *Energy & Environmental Science*, 2016, **9**, 1655-1660.
44. R. Wang, M. Mujahid, Y. Duan, Z.-K. Wang, J. Xue and Y. Yang, *Advanced Functional Materials*, 2019, **29**, 1808843.
45. Y. Yuan and J. Huang, *Accounts of Chemical Research*, 2016, **49**, 286-293.
46. N. E. Courtier, J. M. Cave, J. M. Foster, A. B. Walker and G. Richardson, *Energy & Environmental Science*, 2019, **12**, 396-409.
47. Y. Cao, Y. Li, T. Morrissey, B. Lam, B. O. Patrick, D. J. Dvorak, Z. Xia, T. L. Kelly and C. P. Berlinguette, *Energy & Environmental Science*, 2019, **12**, 3502-3507.
48. J. Zhang, B. Xu, L. Yang, A. Mingorance, C. Ruan, Y. Hua, L. Wang, N. Vlachopoulos, M. Lira-Cantú, G. Boschloo, A. Hagfeldt, L. Sun and E. M. J. Johansson, *Advanced Energy Materials*, 2017, **7**, 1602736.
49. A. Mei, X. Li, L. Liu, Z. Ku, T. Liu, Y. Rong, M. Xu, M. Hu, J. Chen, Y. Yang, M. Grätzel and H. Han, *Science*, 2014, **345**, 295-298.
50. V. Ferguson, S. R. P. Silva and W. Zhang, *ENERGY & ENVIRONMENTAL MATERIALS*, 2019, **2**, 107-118.
51. J. H. Noh, S. H. Im, J. H. Heo, T. N. Mandal and S. I. Seok, *Nano Letters*, 2013, **13**, 1764-1769.
52. E. Edri, S. Kirmayer, D. Cahen and G. Hodes, *The Journal of Physical Chemistry Letters*, 2013, **4**, 897-902.
53. Y. Zhang, Y. Liang, Y. Wang, F. Guo, L. Sun and D. Xu, *ACS Energy Letters*, 2018, **3**, 1808-1814.
54. S. Albrecht, M. Saliba, J. P. Correa Baena, F. Lang, L. Kegelmann, M. Mews, L. Steier, A. Abate, J. Rappich, L. Korte, R. Schlattmann, M. K. Nazeeruddin, A. Hagfeldt, M. Grätzel and B. Rech, *Energy & Environmental Science*, 2016, **9**, 81-88.
55. J. M. Frost, K. T. Butler, F. Brivio, C. H. Hendon, M. van Schilfgaarde and A. Walsh, *Nano Letters*, 2014, **14**, 2584-2590.
56. X. Zheng, B. Chen, M. Yang, C. Wu, B. Orlor, R. B. Moore, K. Zhu and S. Priya, *ACS Energy Letters*, 2016, **1**, 424-430.
57. W. Wang, M. O. Tadé and Z. Shao, *Chemical Society Reviews*, 2015, **44**, 5371-5408.
58. I. Poli, U. Hintermair, M. Regue, S. Kumar, E. V. Sackville, J. Baker, T. M. Watson, S. Eslava and P. J. Cameron, *Nat. Commun.*, 2019, **10**, 2097.

59. N. Arora, M. I. Dar, M. Abdi-Jalebi, F. Giordano, N. Pellet, G. Jacopin, R. H. Friend, S. M. Zakeeruddin and M. Grätzel, *Nano Letters*, 2016, **16**, 7155-7162.
60. S. Rühle, *Solar Energy*, 2016, **130**, 139-147.
61. R. K. Misra, S. Aharon, B. Li, D. Mogilyansky, I. Visoly-Fisher, L. Etgar and E. A. Katz, *The Journal of Physical Chemistry Letters*, 2015, **6**, 326-330.
62. L. Meng, E.-P. Yao, Z. Hong, H. Chen, P. Sun, Z. Yang, G. Li and Y. Yang, *Advanced Materials*, 2017, **29**, 1603826.
63. G. E. Eperon, S. D. Stranks, C. Menelaou, M. B. Johnston, L. M. Herz and H. J. Snaith, *Energy & Environmental Science*, 2014, **7**, 982-988.
64. B. Brunetti, C. Cavallo, A. Ciccioli, G. Gigli and A. Latini, *Scientific Reports*, 2016, **6**, 31896.
65. D. Di Girolamo, M. I. Dar, D. Dini, L. Gontrani, R. Caminiti, A. Mattoni, M. Graetzel and S. Meloni, *Journal of Materials Chemistry A*, 2019, **7**, 12292-12302.
66. A. A. Zhumekenov, M. I. Saidaminov, M. A. Haque, E. Alarousu, S. P. Sarmah, B. Murali, I. Dursun, X.-H. Miao, A. L. Abdelhady, T. Wu, O. F. Mohammed and O. M. Bakr, *ACS Energy Letters*, 2016, **1**, 32-37.
67. X. Yang, X. Zhang, J. Deng, Z. Chu, Q. Jiang, J. Meng, P. Wang, L. Zhang, Z. Yin and J. You, *Nature Communications*, 2018, **9**, 570.
68. F. C. Hanusch, E. Wiesenmayer, E. Mankel, A. Binek, P. Angloher, C. Fraunhofer, N. Giesbrecht, J. M. Feckl, W. Jaegermann, D. Johrendt, T. Bein and P. Docampo, *The Journal of Physical Chemistry Letters*, 2014, **5**, 2791-2795.
69. J. P. Correa Baena, L. Steier, W. Tress, M. Saliba, S. Neutzner, T. Matsui, F. Giordano, T. J. Jacobsson, A. R. Srimath Kandada, S. M. Zakeeruddin, A. Petrozza, A. Abate, M. K. Nazeeruddin, M. Grätzel and A. Hagfeldt, *Energy & Environmental Science*, 2015, **8**, 2928-2934.
70. Q. Jiang, L. Zhang, H. Wang, X. Yang, J. Meng, H. Liu, Z. Yin, J. Wu, X. Zhang and J. You, *Nature Energy*, 2016, **2**, 16177.
71. Y. Liu, Z. Liu and E.-C. Lee, *ACS Applied Energy Materials*, 2019, **2**, 1932-1942.
72. Y. Zhang, S.-G. Kim, D. Lee, H. Shin and N.-G. Park, *Energy & Environmental Science*, 2019, **12**, 308-321.
73. J. Owrut and K. A. Page, *Physical Review B*, 2009, **80**, 195211.
74. B.-X. Chen, H.-S. Rao, W.-G. Li, Y.-F. Xu, H.-Y. Chen, D.-B. Kuang and C.-Y. Su, *Journal of Materials Chemistry A*, 2016, **4**, 5647-5653.
75. D. Shi, V. Adinolfi, R. Comin, M. Yuan, E. Alarousu, A. Buin, Y. Chen, S. Hoogland, A. Rothenberger, K. Katsiev, Y. Losovyj, X. Zhang, P. A. Dowben, O. F. Mohammed, E. H. Sargent and O. M. Bakr, *Science*, 2015, **347**, 519-522.

76. Z. Liu, J. Hu, H. Jiao, L. Li, G. Zheng, Y. Chen, Y. Huang, Q. Zhang, C. Shen, Q. Chen and H. Zhou, *Advanced Materials*, 2017, **29**, 1606774-n/a.
77. Y. Liu, Z. Yang, D. Cui, X. Ren, J. Sun, X. Liu, J. Zhang, Q. Wei, H. Fan, F. Yu, X. Zhang, C. Zhao and S. Liu, *Advanced Materials*, 2015, **27**, 5176-5183.
78. Q. Han, S.-H. Bae, P. Sun, Y.-T. Hsieh, Y. Yang, Y. S. Rim, H. Zhao, Q. Chen, W. Shi, G. Li and Y. Yang, *Advanced Materials*, 2016, **28**, 2253-2258.
79. Q. Cheng, H. Chen, F. Yang, Z. Chen, W. Chen, H. Yang, Y. Shen, X.-M. Ou, Y. Wu, Y. Li and Y. Li, *Angewandte Chemie International Edition*, 2022, **61**, e202210613.
80. N. Arora, M. I. Dar, M. Hezam, W. Tress, G. Jacopin, T. Moehl, P. Gao, A. S. Aldwayyan, B. Deveaud, M. Grätzel and M. K. Nazeeruddin, *Advanced Functional Materials*, 2016, **26**, 2846-2854.
81. Y. Numata, N. Shibayama and T. Miyasaka, *Journal of Materials Chemistry A*, 2022, **10**, 672-681.
82. H. Xu, Z. Liang, J. Ye, S. Xu, Z. Wang, L. Zhu, X. Chen, Z. Xiao, X. Pan and G. Liu, *Chemical Engineering Journal*, 2022, **437**, 135181.
83. J. Kim, T. Hwang, S. Lee, B. Lee, J. Kim, G. S. Jang, S. Nam and B. Park, *Scientific Reports*, 2016, **6**, 25648.
84. H. Chen, X. Zheng, Q. Li, Y. Yang, S. Xiao, C. Hu, Y. Bai, T. Zhang, K. S. Wong and S. Yang, *Journal of Materials Chemistry A*, 2016, **4**, 12897-12912.
85. S. Aharon, B. E. Cohen and L. Etgar, *The Journal of Physical Chemistry C*, 2014, **118**, 17160-17165.
86. C. Wu, D. Wang, Y. Zhang, F. Gu, G. Liu, N. Zhu, W. Luo, D. Han, X. Guo, B. Qu, S. Wang, Z. Bian, Z. Chen and L. Xiao, *Advanced Functional Materials*, 2019, **29**, 1902974.
87. D. Bi, C. Yi, J. Luo, J.-D. Décoppet, F. Zhang, Shaik M. Zakeeruddin, X. Li, A. Hagfeldt and M. Grätzel, *Nature Energy*, 2016, **1**, 16142.
88. J.-S. Zhao, H.-Y. Wang, M. Yu, M.-Y. Hao, S. Yuan, Y. Qin, L.-M. Fu, J.-P. Zhang and X.-C. Ai, *Physical Chemistry Chemical Physics*, 2019, **21**, 5409-5415.
89. R. Lindblad, D. Bi, B.-w. Park, J. Oscarsson, M. Gorgoi, H. Siegbahn, M. Odelius, E. M. J. Johansson and H. Rensmo, *The Journal of Physical Chemistry Letters*, 2014, **5**, 648-653.
90. C. Liu, Z. Huang, X. Hu, X. Meng, L. Huang, J. Xiong, L. Tan and Y. Chen, *ACS Applied Materials & Interfaces*, 2018, **10**, 1909-1916.
91. J. Chen, J. Xu, L. Xiao, B. Zhang, S. Dai and J. Yao, *ACS Applied Materials & Interfaces*, 2017, **9**, 2449-2458.
92. L. Tian, W. Zhang, Y. Huang, F. Wen, H. Yu, Y. Li, Q. Wang, C. Peng, Z. Ma, T. Hu, L. Du and M. Zhang, *ACS Applied Materials & Interfaces*, 2020, **12**, 29344-29356.

93. V. D’Innocenzo, A. R. Srimath Kandada, M. De Bastiani, M. Gandini and A. Petrozza, *Journal of the American Chemical Society*, 2014, **136**, 17730-17733.
94. H. Bian, D. Bai, Z. Jin, K. Wang, L. Liang, H. Wang, J. Zhang, Q. Wang and S. Liu, *Joule*, 2018, **2**, 1500-1510.
95. X. Zheng, B. Chen, J. Dai, Y. Fang, Y. Bai, Y. Lin, H. Wei, Xiao C. Zeng and J. Huang, *Nature Energy*, 2017, **2**, 17102.
96. H. Tsai, W. Nie, J.-C. Blancon, C. C. Stoumpos, R. Asadpour, B. Harutyunyan, A. J. Neukirch, R. Verduzco, J. J. Crochet, S. Tretiak, L. Pedesseau, J. Even, M. A. Alam, G. Gupta, J. Lou, P. M. Ajayan, M. J. Bedzyk, M. G. Kanatzidis and A. D. Mohite, *Nature*, 2016, **536**, 312-316.
97. Y. Lin, Y. Bai, Y. Fang, Z. Chen, S. Yang, X. Zheng, S. Tang, Y. Liu, J. Zhao and J. Huang, *The Journal of Physical Chemistry Letters*, 2018, **9**, 654-658.
98. Y. Zhang, Y. Liu, Z. Xu, H. Ye, Q. Li, M. Hu, Z. Yang and S. Liu, *Journal of Materials Chemistry C*, 2019, **7**, 1584-1591.
99. Q. Jiang, Y. Zhao, X. Zhang, X. Yang, Y. Chen, Z. Chu, Q. Ye, X. Li, Z. Yin and J. You, *Nature Photonics*, 2019, **13**, 460-466.
100. X. Cao, C. Li, Y. Li, F. Fang, X. Cui, Y. Yao and J. Wei, *Nanoscale*, 2016, **8**, 19804-19810.
101. D.-J. Seol, J.-W. Lee and N.-G. Park, *ChemSusChem*, 2015, **8**, 2414-2419.
102. J.-F. Wang, L. Zhu, B.-G. Zhao, Y.-L. Zhao, J. Song, X.-Q. Gu and Y.-H. Qiang, *Scientific Reports*, 2017, **7**, 14478.
103. Y. Liu, Z. Liu and E.-C. Lee, *Journal of Materials Chemistry C*, 2018, **6**, 6705-6713.
104. Z. H. Bakr, Q. Wali, A. Fakharuddin, L. Schmidt-Mende, T. M. Brown and R. Jose, *Nano Energy*, 2017, **34**, 271-305.
105. Q. Fu, H. Liu, S. Li, T. Zhou, M. Chen, Y. Yang, J. Wang, R. Wang, Y. Chen and Y. Liu, *Angewandte Chemie International Edition*, **n/a**, e202210356.
106. H. Zhu, M. B. Johansson and E. M. J. Johansson, *ChemSusChem*, 2018, **11**, 1114-1120.
107. E. H. Jung, N. J. Jeon, E. Y. Park, C. S. Moon, T. J. Shin, T.-Y. Yang, J. H. Noh and J. Seo, *Nature*, 2019, **567**, 511-515.
108. F. De Rossi, G. Renno, B. Taheri, N. Yaghoobi Nia, V. Ilieva, A. Fin, A. Di Carlo, M. Bonomo, C. Barolo and F. Brunetti, *Journal of Power Sources*, 2021, **494**, 229735.
109. G. Kakavelakis, K. Alexaki, E. Stratakis and E. Kymakis, *RSC Advances*, 2017, **7**, 12998-13002.
110. N. Ahn, S. M. Kang, J.-W. Lee, M. Choi and N.-G. Park, *Journal of Materials Chemistry A*, 2015, **3**, 19901-19906.
111. Z. Ku, Y. Rong, M. Xu, T. Liu and H. Han, *Scientific Reports*, 2013, **3**, 3132.

112. B. Turan, J.-P. Becker, F. Urbain, F. Finger, U. Rau and S. Haas, *Nature Communications*, 2016, **7**, 12681.
113. B. A. Pinaud, J. D. Benck, L. C. Seitz, A. J. Forman, Z. Chen, T. G. Deutsch, B. D. James, K. N. Baum, G. N. Baum, S. Ardo, H. Wang, E. Miller and T. F. Jaramillo, *Energy & Environmental Science*, 2013, **6**, 1983-2002.
114. D. Bae, B. Seger, P. C. K. Vesborg, O. Hansen and I. Chorkendorff, *Chemical Society Reviews*, 2017, **46**, 1933-1954.
115. H. Yang, F. Li, X. Wu, P. Zhang, W. Li, S. Cao, Y. Shan and L. Sun, *Electrochimica Acta*, 2018, **281**, 60-68.
116. X. Lu and C. Zhao, *Nat. Commun.*, 2015, **6**, 6616.
117. M. T. Mayer, *Current Opinion in Electrochemistry*, 2017, **2**, 104-110.
118. I. Poli, J. Baker, J. McGettrick, F. De Rossi, S. Eslava, T. Watson and P. J. Cameron, *J. Mater. Chem. A*, 2018, **6**, 18677-18686.
119. S.-W. Lee, S. Kim, S. Bae, K. Cho, T. Chung, L. E. Mundt, S. Lee, S. Park, H. Park, M. C. Schubert, S. W. Glunz, Y. Ko, Y. Jun, Y. Kang, H.-S. Lee and D. Kim, *Scientific Reports*, 2016, **6**, 38150.
120. A. Bard, *Standard potentials in aqueous solution*, Routledge, 2017.
121. Q. Wang, N. Phung, D. Di Girolamo, P. Vivo and A. Abate, *Energy & Environmental Science*, 2019, **12**, 865-886.
122. M. Saliba, M. Stolterfoht, C. M. Wolff, D. Neher and A. Abate, *Joule*, 2018, **2**, 1019-1024.
123. A. Zohar, M. Kulbak, I. Levine, G. Hodes, A. Kahn and D. Cahen, *ACS Energy Letters*, 2019, **4**, 1-7.
124. S. Y. Park and K. Zhu, *Advanced Materials*, 2022, **34**, 2110438.

Acta Universitatis Upsaliensis

Digital Comprehensive Summaries of Uppsala Dissertations from the Faculty of Science and Technology 2268

Editor: The Dean of the Faculty of Science and Technology

A doctoral dissertation from the Faculty of Science and Technology, Uppsala University, is usually a summary of a number of papers. A few copies of the complete dissertation are kept at major Swedish research libraries, while the summary alone is distributed internationally through the series Digital Comprehensive Summaries of Uppsala Dissertations from the Faculty of Science and Technology. (Prior to January, 2005, the series was published under the title "Comprehensive Summaries of Uppsala Dissertations from the Faculty of Science and Technology".)



Distribution: publications.uu.se
urn:nbn:se:uu:diva-500172

ACTA UNIVERSITATIS
UPSALIENSIS
2023